

1 Tsunami hazard in Lombok & Bali, Indonesia, due to the 2 Flores back-arc thrust

3

4 Raquel P. Felix¹, Judith A. Hubbard^{1,2}, Kyle E. Bradley^{1,2}, Karen H. Lythgoe², Linlin Li^{3,4} and
5 Adam D. Switzer^{1,2}

6 ¹Asian School of the Environment, Nanyang Technological University, Singapore

7 ²Earth Observatory of Singapore, Nanyang Technological University, Singapore

8 ³School of Earth Sciences and Engineering, Sun Yat-sen University, Zhuhai, China

9 ⁴Southern Marine Science and Engineering Guangdong Laboratory (Zhuhai), Zhuhai, China

10 *Correspondence to:* Raquel P. Felix (raquelpi001@e.ntu.edu.sg)

11

12 **Abstract.** The tsunami hazard posed by the Flores back-arc thrust, which runs along the northern coast of the
13 islands of Bali and Lombok, Indonesia, is poorly studied compared to the Sunda megathrust, situated ~250 km to
14 the south of the islands. However, the 2018 Lombok earthquake sequence demonstrated the seismic potential of
15 the western Flores Thrust when a fault ramp beneath the island of Lombok ruptured in two Mw 6.9 earthquakes.
16 Although the uplift in these events mostly occurred below land, the sequence still generated local tsunamis along
17 the northern coast of Lombok. Historical records show that the Flores fault system in the Lombok and Bali region
18 has generated at least six \geq M_s 6.5 tsunamigenic earthquakes since 1800 CE. Hence, it is important to assess the
19 possible tsunami hazard represented by this fault system. Here, we focus on the submarine fault segment located
20 between the islands of Lombok and Bali (below the Lombok Strait). We assess modeled tsunami patterns
21 generated by fault slip in six earthquake scenarios (slip of 1-5 m, representing Mw 7.2-7.9+) using deterministic
22 modelling, with a focus on impacts on the capital cities of Mataram, Lombok and Denpasar, Bali, which lie on
23 the coasts facing the strait. We use a geologically constrained earthquake model informed by the Lombok
24 earthquake sequence, together with a high-resolution bathymetry dataset developed by combining direct
25 measurements from GEBCO with sounding measurements from the official nautical charts for Indonesia. Our
26 results show that fault rupture in this region could trigger a tsunami reaching Mataram in <9 minutes and Denpasar
27 in ~23-27 minutes, with multiple waves. For an earthquake with 3-5 m of coseismic slip, Mataram and Denpasar
28 experience maximum wave heights of ~1.6-2.7 m and ~0.6 to 1.4 m, respectively. Furthermore, our earthquake
29 models indicate that both cities would experience coseismic subsidence of 20-40 cm, exacerbating their exposure
30 to both the tsunami and other coastal hazards. Overall, Mataram city is more exposed than Denpasar to high
31 tsunami waves arriving quickly from the fault source. To understand how a tsunami would affect Mataram, we
32 model the associated inundation using the 5m slip model and show that Mataram is inundated ~55-140 m inland
33 along the northern coast and ~230 m along the southern coast, with maximum flow depths of ~2-3 m. Our study
34 highlights that the early tsunami arrival in Mataram, Lombok gives little time for residents to evacuate. Raising
35 their awareness about the potential for locally generated tsunamis and the need for evacuation plans is important
36 to help them respond immediately after experiencing strong ground shaking.

37

38 **1 Introduction**

39 Tsunamis sourced from back-arc thrust faulting, although not as common as megathrust tsunamis, could also
40 result in fatalities and severe damage and destruction to structures. Such are the cases for the Mw 7.7 1991 Limon,
41 Costa Rica (Suárez et al., 1995), Mw 7.9 1992 Flores Island, Indonesia, and Mw 7.5 1999 Ambrym Island of
42 Vanuatu (Regnier et al., 2003) earthquakes. Understanding the tsunami hazard associated with back-arc thrusting
43 is therefore important. Several studies have recognized the contribution of crustal earthquakes, which includes the
44 back-arc thrusting, in the development of tsunami hazard assessments (Selva et al., 2016; Grezio et al., 2017;
45 Behrens et al., 2021).

46

47 Here, we assess the deterministic tsunami hazard associated with the westernmost segment of the Flores Thrust,
48 a back-arc thrust that extends for >1,500 km, accommodating a portion of the convergence between the Indo-
49 Australian and Sunda Plates (Fig. 1a). Unlike its eastern segment, where the 1992 Mw 7.9 Flores Island earthquake
50 occurred, the western part of the fault has not hosted devastating tsunamis in recent years, although historical
51 records and previous studies show that it has generated at least eight tsunamigenic earthquakes (Fig.1b, NOAA
52 database, Hamzah et al., 2000; Rastogi and Jaiswal, 2006; Musson, 2012; Nguyen et al., 2015, Tsimopoulou et
53 al., 2020. The recent 2018 Lombok earthquake-triggered tsunamis were relatively minor because the earthquakes
54 mostly occurred beneath the island itself and not offshore; nevertheless, the occurrence of the 2018 Lombok
55 earthquakes gives new insights into the activity and geometry of this fault segment, and highlights the risk of
56 earthquakes and associated tsunamis along strike.

57

58 Our study focuses on the tsunami hazard caused by slip on the Flores Thrust in the Lombok Strait, a 20-60 km-
59 wide body of water between the islands of Lombok and Bali that connects the Java Sea to the Indian Ocean.
60 Because of its geometry, slip on the thrust in the Lombok Strait could generate tsunamis that would efficiently
61 propagate southwards and hit the west coast of Lombok and the east coast of Bali, where their capital cities
62 (Mataram and Denpasar) are located.

63

64 **1.1 Regional setting**

65 Bali and Lombok islands, east of Java, are part of the Lesser Sunda Islands (Fig. 1a). They are located along the
66 volcanic arc of the Java subduction zone, where the NNE-moving Indo-Australian Plate subducts beneath the
67 Sunda Plate (Dewey and Bird, 1970; Hamilton, 1979; Bowin et al., 1980; Silver et al., 1983, 1986; Hall and
68 Spakman, 2015; Koulali et al., 2016). The Java trench lies ~250 km to the south. The Flores back-arc thrust belt,
69 on the other hand, follows the northern edge of the islands. Here, the kinematics of fault slip and folding are
70 consistent with the sense of movement of the Indo-Australian Plate and associated shortening, indicating that the
71 Flores back-arc thrust also formed to accommodate stress associated with the plate collision (Silver et al., 1983,
72 1986).

73

74 The Flores back-arc thrust is an east-west-trending, south-dipping fault zone that extends for >1,500 km along
75 strike. It is composed of two main segments: the Wetar thrust zone to the east and the Flores Thrust to the west
76 (Silver et al., 1983, 1986; Fig. 1a). From east to west, the Flores Thrust traverses just north of central Flores,
77 Sumbawa, Lombok and Bali (Fig. 1a). From central Flores to east of Lombok, the thrust zone reaches to the

78 seafloor (Silver et al., 1983, 1986; Yang et al., 2020). As the deformation becomes blind from central Lombok to
79 the west, the thrust zone has been mapped based on folds visible in seismic reflection data, and also manifests as
80 a band of steeper north-facing slope on the seafloor (Silver et al., 1983; McCaffrey and Nabelek, 1987; Yang et
81 al., 2020). West of Bali, folds are fewer and have no to little seafloor expression (Silver et al., 1983; Fig. 1d),
82 suggesting that the Flores Thrust terminates at Bali (Yang et al., 2020). However, GPS measurements show that
83 the north-south convergence rate in Bali (5 ± 0.4 mm/yr) is similar to that onshore Java (6 ± 1 mm/yr), therefore
84 back-arc shortening may continue across a segment boundary along the Kendeng thrust in Java (Koulali et al.,
85 2016).

86

87 **1.2 Seismicity of the Flores Thrust**

88 Focal mechanisms show that from February 1976 to February 2021, the Flores Thrust generated 29 Mw 5.5 to 7.8
89 earthquakes within the upper 40 km of the crust (GCMT; Fig. 1a). Earthquakes in this region can be caused by
90 either tectonically driven fault slip or volcanic activity. In this back-arc region, most of the focal mechanisms are
91 characterized by east-west striking nodal planes with a fault plane dipping $26 \pm 8^\circ$ S; we infer that these are
92 associated with the Flores Thrust.

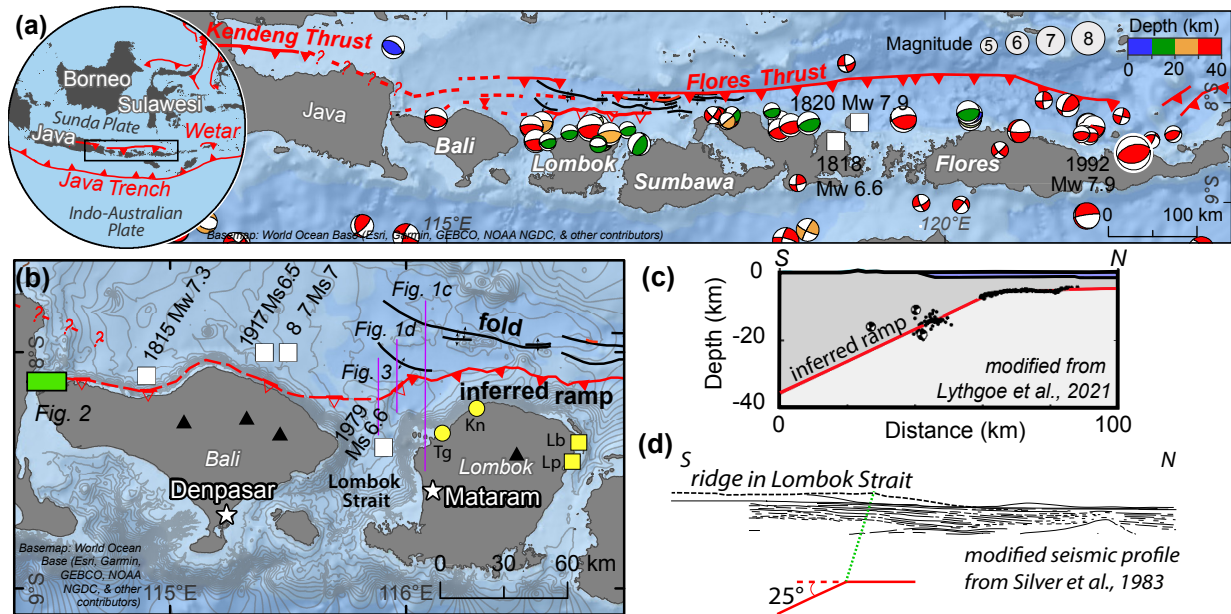
93

94 The activity of this fault system is also testified by uplift recorded on its hanging wall. From eastern Sumbawa
95 to central Flores, uplift is recorded by elevated terraces on the northern sides of the islands (Van Bemmelen,
96 1949). We suggest that the Quaternary reef terraces in northwest Bali (Boekschoten et al., 2000) are also related
97 to tectonic uplift above the Flores thrust system, suggesting that the fault extends all the way to the western
98 coast of the island (Fig. 2).

99

100 Although the earthquakes in this region are largely consistent with tectonic shortening, the active volcanoes not
101 only generate their own seismicity, but also play a role in the horizontal and vertical distribution of fault-generated
102 earthquakes (Lythgoe et al., 2021). A relationship between faulting and volcanic activity was observed for the
103 2018 Lombok earthquake sequence, which generated four $>Mw$ 6 events between 28th July to 19th August. These
104 earthquakes did not occur offshore on the northern frontal thrust of the Flores Thrust, but instead involved slip
105 along the deeper part of the fault and associated imbricate thrusts beneath Lombok, to the north of the active
106 Rinjani volcano (Salman et al., 2020; Yang et al., 2020; Lythgoe et al., 2021). While these earthquakes were not
107 directly caused by volcanic activity, the presence of the volcano constrained the earthquake distribution by
108 elevating the downdip limit of the seismogenic zone in the crust (Lythgoe et al., 2021). Based on relocated
109 earthquakes and seismic reflection data analysis, the earthquakes occurred on the Flores fault ramp, a blind thrust
110 dipping 25° S that flattens updip onto the Flores Thrust décollement at ~ 6 km depth (Lythgoe et al., 2021; Fig. 1c).

111



112

Figure 1: Regional setting of the Flores Thrust and its subsurface ramp-flat geometry. (a) Circle - The Flores back-arc thrust system, which is located along the northern edge of the Lesser Sunda Islands. The thrust is composed of two segments: the Wetar thrust to the east and the Flores Thrust to the west (black rectangle). Seismicity (USGS earthquake catalogue, 1976-2021) and focal mechanism solutions (GCMT, 1976-2021) show that the Flores Thrust is seismically active. The Mw 7.9 Flores Island tsunamigenic earthquake is the largest earthquake on record for this system and occurred at the eastern end of the thrust. (b) The western part of the Flores Thrust has generated historical tsunamigenic earthquakes (white rectangles; www.ngdc.noaa.gov; Hamzah et al., 2000; Rastogi and Jaiswal, 2006; Musson, 2012; Nguyen et al., 2015; Griffin et al., 2019). Yellow squares and circles: towns where a tsunami was reported following the Mw6.4 28th July and Mw6.9 5th Aug 2018 events, respectively. Tg – Tanjung, Kn – Kayangan, Lb – Labuhan Pandan and Lp – Leper. We interpret that the blind ramp mapped at Lombok (Lythgoe et al., 2021) extends westwards based on the seafloor morphology and uplifted terraces in the northwestern part of Bali (green rectangle; Fig. 2). Basemaps – World Ocean Base. The map extent of (b) reflects the coverage of grid layer 1 (L1) used in the tsunami modelling. The basemap of (b) with only contour lines overlain is shown on Fig. S1. (c) The geometry of the blind fault ramp is constrained by the seismicity of the 2018 Lombok earthquake sequence (Lythgoe et al., 2021). (d) Gentle folds interpreted by Silver et al., (1983) based on a seismic profile across the Lombok Strait. Below the profile we show our inferred location for the fault ramp.

113

114 1.3 Tsunamigenic earthquakes of the Flores Thrust

115 Historical records (NOAA database, www.ngdc.noaa.gov) and tsunami studies (Hamzah et al., 2000; Rastogi and
 116 Jaiswal, 2006; Musson, 2012; Nguyen et al., 2015; Griffin et al., 2019) document at least four tsunamigenic
 117 earthquakes on the Flores Thrust, in addition to the two earthquakes in 2018, which produced local inundation
 118 (Fig. 1b). Three of these events occurred in the western part of the thrust zone, north of Bali. The oldest event on
 119 record is the 1815 Ms 7 earthquake, which triggered a landslide and tsunami; together, these events killed >1,200
 120 people. NOAA categorizes this as a probable tsunamigenic event, as it is unclear whether the tsunami was caused
 121 only by the coastal landslide, or by the earthquake and landslide together. The 1857 Ms 7 and 1917 Ms 6.5 events
 122 are described by NOAA as definite and probable tsunamigenic earthquakes, respectively. The 1857 event
 123 generated four consecutive tsunami waves, at least 3 m high, northwest of Flores Island (National Geophysical

124 Data Center / World Data Service: NCEI/WDS Global Historical Tsunami Database. NOAA National Centers for
125 Environmental Information. doi:10.7289/V5PN93H7). In addition, in the Lombok Strait, a 1979 Ms 6.6
126 tsunamigenic earthquake left 200 injured and killed 27 people, although the tsunami is poorly documented and
127 may have played a minor role in the destruction (Hamzah et al., 2000).

128

129 The best-documented tsunamigenic earthquake on the Flores Thrust occurred in its far eastern part
130 (Yeh et al., 1993; Imamura and Kikuchi, 1994; Tsuji et al., 1995; Pranantyo et al., 2021). The 1992 Mw 7.9 Flores
131 Island earthquake injured 2,144 people and killed 2,080 (Yeh et al., 1993; Tsuji et al., 1995; Fig. 1a). This
132 earthquake occurred at ~16 km depth (Beckers and Lay, 1995), and generated a tsunami that propagated to the
133 northern coast of Flores Island within five minutes (Yeh et al., 1993). Field mapping shows that the tsunami
134 inundated the land as far as 600 m, with an average run-up height of ~2 to 5 m (elevation reached above sea level).
135 Anomalously high run-up heights of 20-26 m to the northeast may be associated with submarine landslides (Yeh
136 et al., 1993).

137

138 The recent 2018 Lombok earthquake sequence occurred primarily below land, but nevertheless small-scale
139 tsunamis were reported by the residents of northern Lombok (Tsimopoulou et al., 2020). When the Mw 6.4 July
140 event occurred, the northern coast of Lombok subsided by ≤ 0.1 m (Wibowo et al., 2021), and the northeastern
141 coast was hit by a tsunami at the towns of Labuhan Pandan and Tanjung, which were inundated 10-70 m with
142 run-up heights of ~1-2.5 m. For the Mw 6.9 August 5 event, although the northern coast was uplifted by ≤ 0.5 m
143 (Wibowo et al., 2021), the residents of the northwest towns, Tanjung and Kayangan, reported a tsunami that
144 inundated 7-40 m inland with a run-up height of ~1.7-2 m (Fig. 1b).

145

146 Together, these records show that the Flores Thrust is capable of generating significant thrust earthquakes with
147 associated land uplift/subsidence as well as local tsunamis. The full tsunamigenic potential of this fault system is
148 not known, as the observational window is short compared to typical earthquake recurrence intervals. Here, the
149 observational window refers to the historical and seismic records. To our knowledge, there are no paleo-tsunami
150 studies in this area that are associated with the Flores Thrust. There is a paleo-deposit study in Bali, but it is
151 interpreted to be deposited by a tsunami generated by the megathrust rupture (Sulaeman, 2018). Hence, we rely
152 only on historical and seismic records when we refer to a short observational window. The tsunami studies related
153 to Flores Thrust are limited and they are about the numerical modelling of the historical tsunamis. Here, we
154 explore what could happen when coseismic slip occurs on the Flores thrust ramp within the Lombok Strait, and
155 how the generated tsunami and coseismic land deformation would together affect the coastal cities of Mataram,
156 Lombok and Denpasar, Bali.

157

158

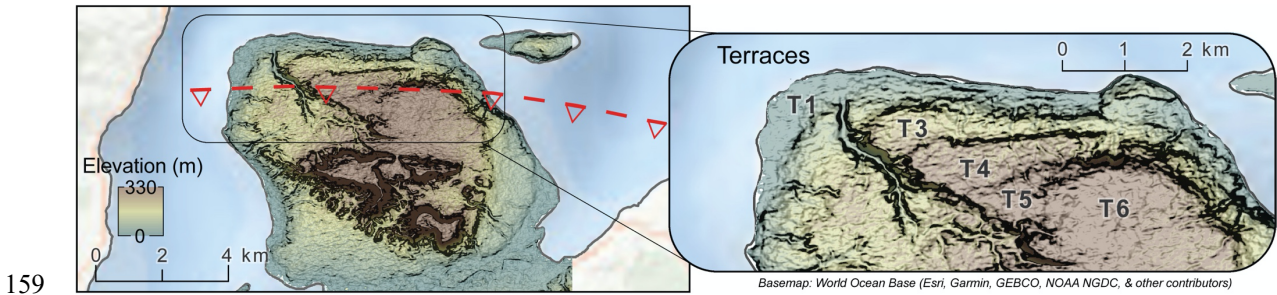


Figure 2: Six coastal terraces (T1-T6) identified using a digital elevation model (DEMNAS) in northwest Bali, likely uplifted due to slip on the Flores Thrust ramp. The location is shown as a green rectangle on the map in Figure 1b. Basemap – World Ocean Base.

160

161 1.4 Previous tsunami modelling studies

162 Tsunami modelling studies in this region commonly focus on the segment of the Sunda Megathrust along the
 163 Java trench (Okal and Borrero, 2011; Kurniawan and Laili, 2019; Suardana et al., 2019; Kardoso and Dewi, 2021)
 164 (Fig. 1a), with a few studies evaluating the western segment of the Flores Thrust (Rusli et al., 2012; Løvholt et
 165 al., 2012; Afif and Cipta, 2015), and four considering an earthquake sourced within the Lombok Strait (Rakowsky
 166 et al., 2013; Horspool et al., 2014; Pradjoko et al., 2018; Wibowo et al., 2021; Fig. 1b). All four studies show
 167 tsunami results in Mataram, Lombok; however, each study focuses on different aspects of tsunami modelling, and
 168 three predate the 2018 Lombok earthquake sequence, which illuminated important aspects of the fault geometry.
 169 The only study after the 2018 earthquakes (Wibowo et al., 2021) did not update their fault model to reflect new
 170 information about the geometry of the Flores Thrust derived from studies of the 2018 Lombok earthquake
 171 sequence. Overall, these prior results do not address the potential earthquake scenarios that we consider plausible:
 172 Rakowsky et al. (2013) study the sensitivity of inundation to land friction, Horspool et al. (2014) describe the
 173 probabilistic tsunami hazard, Pradjoko et al.(2018) considers a fault that is much too steep and uses bathymetry
 174 that is too coarse to produce reliable results, and Wibowo et al. (2021) did not consider the post-2018 earthquake
 175 studies of the fault geometry of the Flores Thrust.

176

177 Rakowsky et al. (2013) studied the sensitivity of inundation models in the region to the topography and friction
 178 parameters of the land surface. Their tsunami modeling was done using the ~900-m-resolution GEBCO dataset
 179 interpolated with measurements from ships and nautical charts; the interpolation method is not described in detail.
 180 They considered a Mw 8.5 earthquake and produced a maximum flow depth (vertical distance between the land
 181 and inundating water surface) of 10 m, with an inundation extent ranging from ~1-1.6 km in Mataram. This
 182 earthquake magnitude is larger than any observed event as the most recent estimates of the historical tsunamigenic
 183 earthquakes in the Flores Thrust ranges from Mw 6.6 to Mw 8.3, (Griffin et al., 2019), and that seismic records
 184 show that the 1992 Flores Island earthquake is Mw 7.9. They found that inundation distance depended on the
 185 topographic parameters: lower bottom friction or a bare earth digital terrain model produced higher inundation
 186 compared to higher friction or a digital surface model (with structures, e.g., houses). Their results highlight the
 187 importance of using an accurate surface model when assessing potential inundation.

188

189 Horspool et al. (2014) focused on probabilistic tsunami hazard for all of Indonesia. They used a bathymetry dataset
190 that combined GEBCO data with measurements from Navy charts and multibeam surveys. The maximum
191 magnitude calculated for the Flores thrust is Mw 8.1, Mw 8.3 and Mw 8.5 for fault dips of 25-27°. Their results
192 do not describe the regional hazard (e.g. wave heights, timing, inundation), but rather assess how much of the
193 local hazard is contributed by this fault system rather than the megathrust. They showed that for a 500-year return
194 period, the tsunami hazard in Mataram is 10-30% most likely due to the shallow part of the Flores Thrust.

195

196 Pradjoko et al. (2018) used a model of a Mw 6.4 earthquake to simulate a scenario similar to the 1979 event,
197 which was the largest recorded earthquake in this region prior to the 2018 Lombok earthquake sequence. They set
198 2.5 m of fault slip on a 72°-dipping fault (significantly steeper than the 25° dip we interpret for the fault) centered
199 at 25 km depth. Using GEBCO bathymetry to model tsunami propagation (with a coarse horizontal resolution of
200 ~900 m), their results indicate that a Mw6.4 earthquake could generate a 0.13-0.2 m-high tsunami wave that
201 arrives at the coast of Mataram ~18-20 minutes after the earthquake.

202

203 The study by Wibowo et al. (2021) focused on the tsunami hazard posed by a Mw 7.4 earthquake on the Flores
204 thrust to the northern coasts of Lombok and Bali. They set 2.7 of slip on a 27°-dipping fault plane with dimensions
205 of 75 km x 27 km centered at 27 km depth. The fault parameters they used are based on the mean values of the
206 earthquake sources in the USGS 1900-2020 earthquake database. The orientation and depth of the fault are similar
207 to those we use in our modeling, but the updip tip of the fault in their model is located about 25 km north of the
208 islands rather than along the northern coast of the islands, as we interpret from the 2018 Lombok earthquake
209 sequence and bathymetry in the Strait. They used the 180-m resolution National Bathymetry of Indonesia
210 (BATNAS) dataset as input bathymetry in the numerical simulations. Their focus was on the impact along the
211 northern coasts, but they note that the tsunami arrives in Mataram and Denpasar in 9 and 25 minutes, respectively.
212 They also find that the maximum wave height is 1.5 m in Mataram and 1 m in Denpasar.

213

214 Following the 2018 Lombok earthquake sequence, we now have a more accurate understanding of the location
215 and subsurface geometry of the Flores Thrust in this region. Hence, the earthquake models we use in our study
216 are geologically well-constrained. In addition, since tsunami propagation in shallow water depends strongly on
217 the bathymetry, we develop and incorporate a new bathymetric model by combining the GEBCO dataset with
218 sounding measurements from the official nautical chart for Indonesia. This is particularly important along the
219 shallow coast, where seafloor roughness has a strong control on wave propagation. In our study, we show the
220 tsunami results from six different earthquake scenarios within the Lombok Strait, highlighting impacts on the
221 populated capital cities of Mataram, Lombok and Denpasar, Bali, as both cities face the Strait. We also calculate
222 the coseismic uplift and subsidence for varying slip amounts, and report this together with the tsunami time history
223 and pattern and the maximum wave height. An inundation scenario is also included for the city of Mataram.

224

225 **2 Methodology**

226 **2.1 Fault model setup**

227 The 2018 Lombok earthquake sequence illuminated the geometry of the Flores Thrust beneath Lombok (Fig. 1c).
228 Together, relocated aftershocks, earthquake slip distributions, and seismic reflection imaging indicate a blind fault

229 ramp dipping 25°S that flattens updip to a décollement at ~6 km depth and continues north below the Bali Sea.
 230 The part of the thrust ramp that ruptured in the 2018 sequence extends 45 km downdip and 116 km lengthwise
 231 (Lythgoe et al., 2021; Fig. 1c & 3).

232 We use these fault parameters to set up our fault model, choosing a fault with an east-west strike, similar to the
 233 general trend of the Flores Thrust, positioned across the Lombok Strait. The complete parameters are listed in
 234 Table 1. We are not trying to replicate the 2018 earthquakes, but rather consider an earthquake on the neighboring
 235 part of the fault that did not rupture in that sequence. The eastern boundary of the fault model slightly overlaps
 236 with the western limit of the 2018 earthquake sequence. Such overlapping ruptures have been observed in Kuril
 237 Trench (Ammon et al., 2008) and Peru-Chile Trench (Bilek, 2010). We extend the western edge of the model to
 238 below the eastern edge of Bali, in order to span the width of the Strait; the fault likely continues further west (as
 239 evidenced by uplifted terraces and seismicity), but rupture to the west would occur below land and would not
 240 contribute to a tsunami. As there are limited available information on the structural geology and the seismicity of
 241 the Flores Thrust in this region, While there is limited data within the strait to assess the continuity of the fault,
 242 there is no reason to believe that there are significant structural variations along strike. The focal mechanisms for
 243 the events near Bali have very similar strike and dip to that at Lombok (Fig. 1a). When varying the fault dips to
 244 18° and 34°, representing the minimum and the maximum limits of the fault dip uncertainty, they have minimal
 245 impact on the tsunami model. The tsunami energies inherent in these two models are only 5-8% different from
 246 the energy of our model with a 25° fault dip (Felix et al., 2021). Hence, minor structural variations would result
 247 in minor changes in arrival times and wave heights but would not be likely to have a strong effect on our results.

248 **Table 1: Parameters of fault models A and B used in the numerical modelling.**

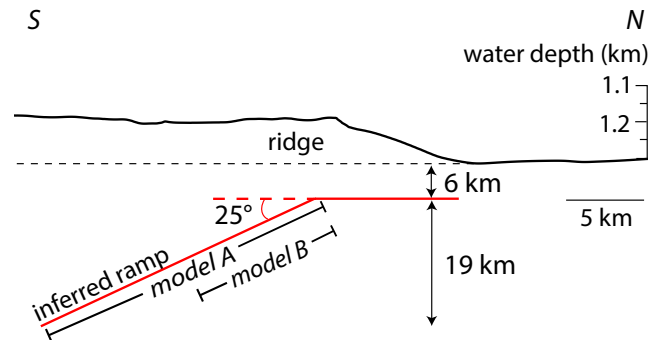
| Parameters | Fault model A | Fault model B |
|---------------------|---------------|---------------|
| Epicenter longitude | 115.77° E | 115.77° E |
| Epicenter latitude | 8.3821° S | 8.2905° S |
| Focal depth | 15.5 km | 10.8 km |
| Width | 45 km | 22.5 km |
| Length | 116 km | |
| Strike | 90° E | |
| Dip | 25° S | |
| Rake | 90° | |

249

250 We trace the upper blind tip of the fault ramp following the southern edge of a north-facing seafloor slope. This
 251 surface morphology coincides with folding interpreted from seismic reflection surveys (Silver et al., 1983; Yang
 252 et al., 2020), and we interpret that the folding formed due to slip across a bend at the upper tip of the blind fault
 253 ramp (Fig. 1b). We extend the fault ramp to a depth of 25 km below the seafloor, which represents the maximum
 254 seismogenic depth in this region based on historical seismic records and the maximum depth of seismicity
 255 observed in the 2018 sequence (Lythgoe et al., 2021).

256 We model two fault ruptures on this fault (Models A and B, Fig. 3). Model A consists of a whole-fault rupture,
 257 while Model B allows only the upper half of the ramp to slip. This second model represents a scenario similar to

258 the 2018 Lombok earthquakes, where most of the slip occurred on the shallow part of the fault ramp. However,
 259 the maximum rupture depth at Lombok was interpreted to be limited by the elevated geothermal gradient
 260 associated with the volcano. In the Lombok Strait, there is no such volcano; thus, it is likely that slip within the
 261 Lombok Strait could reach deeper due to the colder geothermal gradient.



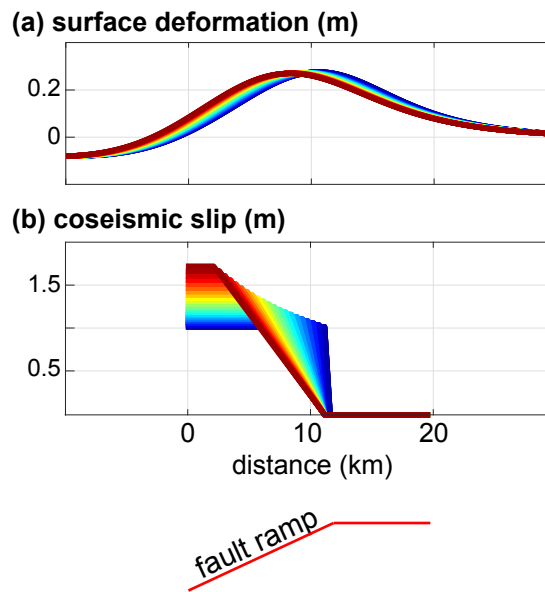
262

Figure 3: Profile of the fault geometry used in the tsunami modelling relative to the seafloor ridge. We study two fault slip models: model A (whole-ramp rupture) and model B (slip only on the upper half of the ramp). The location of the profile is shown in Fig. 1b.

263 2.2 Slip model

264 For both Models A and B, we consider three deterministic scenarios with uniform slip of 1, 3, and 5 m (six
 265 scenarios total). The modeled historical tsunamigenic earthquakes in the Flores Thrust are estimated to have
 266 magnitudes ranging from Mw 6.7 to Mw 8.5 (NOAA, Musson et al., 2019; Griffin et al., 2019). Using the
 267 scaling relationship for magnitude and slip of shallow crustal reverse faulting by Thingbaijam et al. (2017),
 268 these earthquake magnitudes have average slip ranging from 1 to 5 m. In order to represent this range, we use
 269 the minimum (1 m), the mid-range (3 m) and the maximum (5 m) slip values in our modelling. In the
 270 subsequent texts, we refer to these slip models as A-1, A-3 and A-5 for fault model A and B-1, B-3 and B-5 for
 271 fault model B. We note that although modelling with more complex rupture scenarios would perhaps be a more
 272 detailed option (e.g. Serra et al., 2021), the current information that we have about the Flores Thrust in Bali and
 273 Lombok region, however, is limited. Hence, we think that it is better to use a planar fault model and uniform
 274 slip to lessen the use of random parameters that could increase the uncertainty in the results. We also note that
 275 although probabilistic approaches are becoming more common, the deterministic method is still included in
 276 recent tsunami hazard studies (e.g. Wronna et al., 2015; Roshan et al., 2016; Gonzales, et al., 2019; Escobar et
 277 al., 2020; Rashidi et al., 2020; Hussain et al. 2021; Rashidi et al., 2022).

278 In order to focus on the impact of tsunami generation, we include only slip on the fault ramp (no slip transferred
 279 onto the northern décollement). This updip termination of slip was observed in the Lombok sequence (Lythgoe et
 280 al., 2021) and is therefore realistic in our region to the west as well. Although we consider uniform slip, earthquake
 281 slip is known to be spatially variable, and in particular to taper around the edges of the slip patch. We evaluate the
 282 impact of this taper on the initial seafloor deformation using the Green's function for rectangular dislocations
 283 (Okada, 1992) in the code Unicycle (Moore et al., 2019); we find that tapering the slip slightly modifies the uplift
 284 profile by broadening it and shifting it to the south (downdip direction) but does not significantly change the
 285 model (Fig. 4).



287

288 **Figure 4: Influence of tapering the updip slip on seafloor deformation. The maximum slip varies across the models in**
 289 **order to preserve the mean slip. (a) The seafloor deformation profiles have similar amplitudes and shapes with slightly**
 290 **offset peaks, even for very significant tapers. (b) Different slip tapers considered. A more gradual taper (red shades)**
 291 **shifts the peak uplift in the downdip direction of the fault ramp. A more abrupt slip taper (blue shades) shifts the peak**
 292 **uplift towards the upper fault bend.**

293 To better translate the models into equivalent earthquakes, we calculate the equivalent Moment Magnitude (M_w)
 294 for each modeled event, using a rigidity of 35 GPa and 30 GPa for models A and B, respectively. These are the
 295 mean rigidities calculated from the values, presented in Sallarès and Ranero (2019) and Sallarès et al. (2021),
 296 every 1 km interval from 6 to 25 km depths for Model A, and from 6 km to 15.5 km depth for model B. Since
 297 Model A has a wider fault surface, for the same amount of slip, it produces larger magnitudes compared to Model
 298 B (Table 2). In each model, we consider only the part of the fault that lies below the Lombok Strait, since this is
 299 the part of the fault that is submarine and therefore capable of generating tsunamis. We note that an earthquake
 300 rupturing this fault segment could involve slip further along strike, either to the west (below Bali) or to the east
 301 (below Lombok, although this part of the fault recently ruptured in multiple earthquakes and is relatively less
 302 likely to slip again). Indeed, reaching 5 m of slip within the Lombok Strait alone would likely require a longer
 303 rupture, and therefore a larger magnitude than the values reported in Table 2, given known scaling relationships
 304 between fault area and coseismic slip (Thingbaijam et al., 2017).

305 **Table 2: Equivalent Moment Magnitudes (M_w) for Models A and B for a given slip amount. Model A**
 306 **ruptures the full ramp while Model B ruptures only the upper half of the ramp. Both models have a fault**
 307 **length of 116 km. The magnitudes here are minima, as each of these events could also include slip on the**
 308 **along-strike part of the fault.**

309

| | Model A | Model B |
|--|--------------------|----------------------|
| | Fault width: 45 km | Fault width: 22.5 km |

| Slip (m) | Mw | |
|----------|-----|-----|
| 1 | 7.5 | 7.2 |
| 3 | 7.8 | 7.5 |
| 5 | 7.9 | 7.7 |

310

311 2.3 Bathymetry

312 Accurate modeling of tsunami wave propagation requires a high-resolution bathymetric map, especially in shallow
313 water. By using detailed bathymetry together with a fine grid size, modelled simulations of tsunami wave heights
314 have been shown to effectively match real near-coast waveforms (Satake, 1995). However, in many parts of the
315 world, high resolution bathymetric data are unavailable. In general, regional tsunami studies use only one
316 bathymetric dataset (e.g., Satake, 1988), commonly either ETOPO (<https://www.ngdc.noaa.gov/mgg/global/>) or
317 GEBCO (<https://www.gebco.net/>), because they are publicly available and have wide coverage. However, these
318 datasets have an artificially smooth seafloor (Marks and Smith, 2006), especially at shallow depths, because of
319 the low density of interpolated points (e.g., Fig. 5). In local tsunami studies, the detailed seafloor morphology in
320 shallow water is critical, since seafloor roughness in these regions has nonlinear effects on wave propagation
321 (Wang and Power, 2011). Kulikov et al. (2016) demonstrated that tsunami propagation modeled using the GEBCO
322 dataset results in substantial errors in the estimation of wave propagation.

323

324 We generate a high-resolution bathymetric model of the region of interest by combining water depth
325 measurements from GEBCO with sounding measurements from the official nautical charts of Indonesia
326 (<http://hdc.pushidrosal.id/>). The publicly available GEBCO dataset is provided as an interpolated raster, but also
327 includes the original data points used for interpolation. These data points (water depths) are derived from a variety
328 of sources, both direct (echo soundings, seismic reflection, isolated soundings, electronic navigation chart
329 soundings) and indirect (e.g. satellite altimetry, flight-derived gravity data). Using the Type-Identifier Grid file
330 from GEBCO, which includes the source of the depth data, we identify and extract only the water depths acquired
331 by direct measurement (Fig. 5).

332

333 The GEBCO data in this region are concentrated along the heavily-travelled ship tracks between the islands of
334 Bali and Lombok, and are too low resolution near the coasts to accurately model tsunami propagation and wave
335 heights (Fig. 5a). We improve the resolution of our bathymetry by digitizing sounding data from the official
336 nautical charts of Indonesia, which are densest in the coastal regions near the cities of Denpasar (Bali) and
337 Mataram (Lombok) and therefore critical for modeling near-shore wave heights in these regions (Fig 5b). We also
338 trace the coastline using the National Digital Elevation Model (DEMNAS, <http://tides.big.go.id/DEMNAS/>), and
339 cross check it using satellite images from Esri World Imagery (<https://www.arcgis.com/>).

340

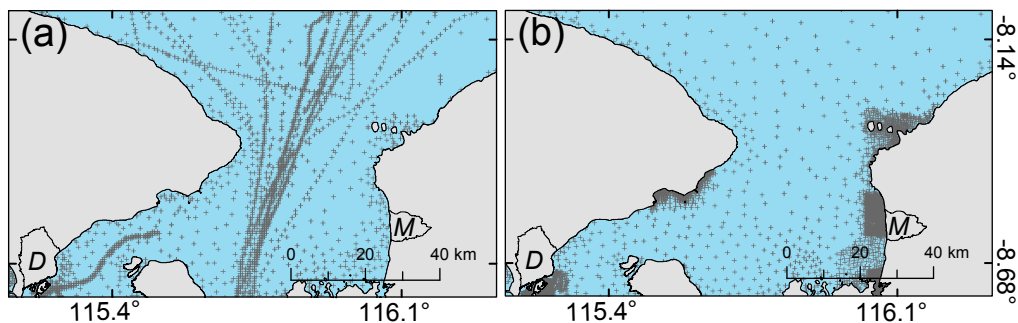
341 We combine the water depth measurements from both sources and the coastlines into a single dataset, and then
342 interpolate the data using the ‘Topo to Raster’ tool in ArcGIS. This tool is based on the ANUDEM program
343 developed by Hutchinson (1989), and generates a continuous digital elevation model based on point data that
344 takes into account the hydrological correctness of the resulting raster. While this method was developed on the
345 basis of subaerial water flow, it has also been used to effectively generate bathymetries for tsunami studies in

346 other regions (Fraser et al., 2014; Darmawan et al., 2020; Wilson and Power, 2020). We note that the shallow
347 shelf regions of the Lombok Strait were likely incised subaerially during the late Holocene sea-level drop
348 (Boekschoten et al., 2000), and their morphologies therefore likely reflect subaerial water flow processes.

349

350 We set the resolution of our interpolated raster to 30 m, as this is similar to the mean distance between the data
351 points along the coasts of Mataram (~27) and Denpasar (~36 m). Our final bathymetry represents a reasonable
352 balance between achievable accuracy at shallow depths and computational efficiency. We validate the interpolated
353 bathymetry by comparing its values with the source data; the mean difference in the shallow regions offshore
354 Mataram and Denpasar is <0.4 m.

355



356

357 **Figure 5: Comparison of the point density of water depth measurements from (a) GEBCO (direct measurements) and**
358 **(b) nautical charts (soundings). GEBCO data are densest along the center of the Lombok Strait (following ship tracks),**
359 **while the nautical chart soundings are concentrated near the coastal cities. Combining these data points enhances the**
360 **accuracy of the resulting bathymetry (shown in Fig. 6). Crosses – locations of measurements. Polygons on land – cities**
361 **of Denpasar, Bali and Mataram, Lombok. D = Denpasar, M = Mataram.**

362

2.4 Topography in Mataram, Lombok

363 Based on our tsunami model runs, the highest wave heights are observed along the coast of Mataram, Lombok.
364 In order to further explore the tsunami hazard in this populated area (Fig. 6), we model the inundation of the
365 onshore region. The inundation distance and run-up height of a tsunami can vary significantly depending on
366 factors such as the average slope of the coast and the land cover roughness (Kaiser et al., 2011; Griffin et al.,
367 2015); an accurate forecast requires a high-resolution Digital Surface Model (DSM) that maps the buildings and
368 trees.

369

370 We use a Digital Surface Model generated by Apollo Mapping based on Pleiades satellite imagery. The DSM has
371 a horizontal resolution of 1.5 m and a vertical error of ± 3 m. This vertical error is the lowest possible for digital
372 elevation models without ground control points, which we do not have access to. We use a DSM rather than a
373 DTM (Digital Terrain Model) to better represent the man-made structures (e.g., houses, infrastructure) present in
374 Mataram city. There are a few areas where the DSM is unavailable along the coast, due to difficulties in data
375 processing associated with tides. We fill these areas with 1.5-m resampled elevation data from DEMNAS, the
376 national elevation model for Indonesia, which has a coarser original horizontal resolution of 8 m. The vertical
377 datum of the merged data is referenced to EGM2008.

378

379 In order to run the inundation modelling, the topographic data must be merged with the bathymetry so that the
380 incoming wave can be smoothly modeled across the sea-land interface. To match the resolution of the DEMNAS-
381 DSM model, we generate another bathymetry model with 1.5 m resolution in the Mataram region using the same
382 'Topo to Raster' interpolation method as used previously for the bathymetry. We match the coastlines of the two
383 datasets to generate the final combined model.

384

385 **2.5 Tsunami modelling using COMCOT**

386 We model the tsunami generation, propagation, run-up and inundation using the Cornell Multi-grid Coupled
387 Tsunami (COMCOT) model developed by Liu et al. (1995). This modeling system solves linear and nonlinear
388 shallow water equations using a modified leap-frog finite difference approach (Wang & Power, 2011). It uses a
389 nested-grid layer algorithm to increase its computational efficiency. The Okada (1985) model is used to calculate
390 surface deformation due to fault slip. We use this model in our study as it has been extensively adopted and
391 validated for modelling tsunami events (e.g., 1960 Mw 9.5 Chilean tsunami – Liu et al. 1995; 2004 Mw 9 Indian
392 Ocean Tsunami - Wang and Liu, 2007; 2006 Mw 7.7 South Java tsunami – Tri Laksono et al. 2020; 2010 Mw 7.8
393 Mentawai earthquake – Hill et al. 2012; 2011 Tohoku tsunami – Chau and Lam, 2015).

394

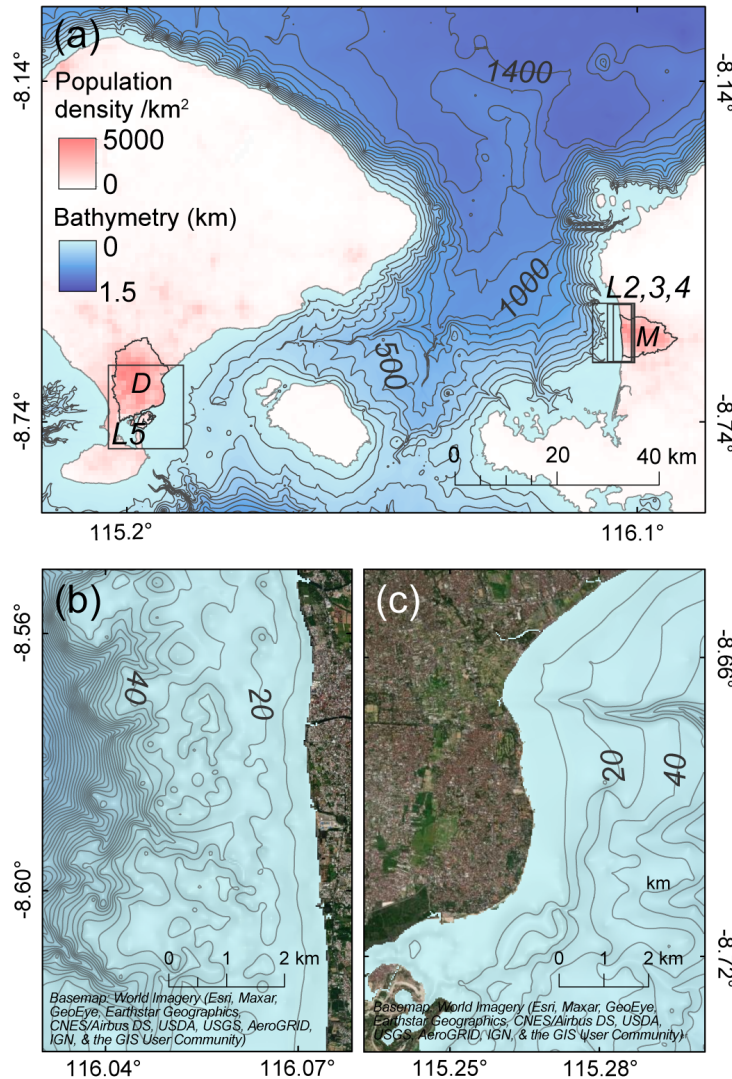
395 For our tsunami modelling, we set up a total of six grid layers in a spherical coordinate system, with finer
396 resolution in the shallow regions along the coasts of Mataram and Denpasar (Fig. 6). For the parent grid layer
397 (L1), the extent covers the entire islands of Bali and Lombok (shown as the extent of Fig. 1b) and its grid size is
398 set to 150 m. We use 3 nested grid layers in Mataram with resolutions of 30 m (L2), 6 m (L3) and 1.5 m (L4, Fig.
399 6), while we use 1 sublayer in Denpasar with a grid size of 30 m (L5, Fig. 6). We added a 1.5 m grid size resolution
400 in Mataram to simulate the inundation of model A-5, representing the “worst case” of our various models. This
401 does not necessarily mean that it gives the worst-case tsunami scenario, and that a lower magnitude earthquake
402 can generate a comparable tsunami (Salaree et al., 2021). We only use one earthquake scenario because high
403 resolution inundation modeling is computationally expensive. Linear and nonlinear shallow water equations are
404 used on L1 and L2-L5, respectively. We set the Manning’s roughness coefficient in L3-L5 to 0.013 on the water
405 region, and 0.03 on land (Wang and Power, 2011). The results of the simulations in grid layer L1 are shown on
406 Figures 7 and 8, and the results in L2 and L5 are shown on Figures 9-11. The simulations in L4 are shown as
407 inundation maps on Figures 12 and 13.

408

409 We run the tsunami simulation from the time of the earthquake for one hour; this is sufficient to capture both the
410 first wave and a series of smaller, later waves, since the coastal regions we are interested in are close to the source
411 (<100 km). To observe the tsunami arrival pattern along the coasts of Mataram and Denpasar within the hour, we
412 select virtual tide gauge locations along the 10-m bathymetric contour, facing the coastal areas where dense man-
413 made structures are identified from satellite images. The results of the tsunami modeling are illustrated using maps
414 of the initial sea surface deformation, maximum wave height, coseismic land subsidence in Bali and Lombok,
415 time series of wave arrivals at the virtual tide gauges, and maps of inundation depth in Mataram.

416

417



418

Figure 6: The generated bathymetry in the Lombok Strait. (a) The bathymetry has a north-south trending ridge along a narrow path between Bali and Lombok with its base at 1.4 km water depth, which is the deepest water depth in this region. The extent of (a) matches the extent of grid layer L1 used in the tsunami modelling. The finer grid layers L2-L4 and L5 are focused on the populated cities of Mataram and Denpasar, respectively. M = Mataram, D = Denpasar. Grid resolutions: L1 = 150 m; L2 and L5 = 30 m; L3 = 6 m, and L4 = 1.5 m. The population density is from worldpop.org (Bondarenko et al., 2020). (b) The linear coast of Mataram faces a rugged but gently dipping seafloor that suddenly steepens ~3-4 km from the coast. (c) Denpasar city has a more complex coastline and a smoother seafloor. Basemaps – World Imagery.

419 **3 Results**

420 **3.1 Coseismic deformation and maximum wave height**

421 When slip occurs on the Flores Thrust ramp during an earthquake, the elastic response of the crust will lead to
 422 broad changes in the elevation of the ground surface. In the north, above the fault ramp, the seafloor will rise
 423 (uplifting any ocean column above), whereas the southern region will subside (Fig. 7a-c). Associated with this
 424 process, the islands of Bali and Lombok will tilt towards the south (Fig. 7a-c, 8a-c). As the initial sea surface

425 deformation will have the same magnitude as the land deformation, the initial wave will be unnoticeable relative
426 to the coast, which experiences the same vertical motion (Fig. 7d-f, 8d-f). As the fault patches of our fault models
427 A (45 km) and B (22.5 km) are much larger than the ~ 1.4 km maximum water depth in Lombok Strait, we note
428 that the dispersion effect due to the water column (Kajiura, 1963) is not included here. The energy transmitted to
429 the sea surface from the seafloor by our models is only 2-3% different from the filtered versions (Felix, et. al.,
430 2021). The initial waves in our models correspond to tsunami energies of 1, 13, and 36 TJ for Model A and 1, 7,
431 and 20 TJ for Model B for 1, 3, and 5 m of slip, respectively (Felix et al., 2021).

432 The coseismic land change and tsunami heights are influenced by the distance from the fault and the shape of the
433 coastline. Lombok and Bali have east-west trending headlands at 8.38°S latitude. In Lombok, the less protruding
434 headland connects southwards to a north-south-trending linear coastline. In Bali, on the other hand, the headland
435 protrudes further and connects to a southeast-facing coastline with a curved morphology. When the full fault slips
436 (model A), the northern half of the islands, including the headlands at 8.38°S , are uplifted (Fig. 7). This uplift acts
437 to counter any transient waves, including the initial wave, and results in a maximum relative wave height of
438 generally <0.5 m along the northern coasts. The exception is the headlands, where the waves can be much higher;
439 here, the waves refract towards the concave coastlines, and the wave heights can reach ~ 1 - 1.9 m high for models
440 A-3 and A-5 (Fig. 7d-e).

441 Along the southern coasts, on the other hand, coseismic subsidence acts to increase the relative tsunami heights.
442 The subsidence in southern Lombok and Bali can reach as high as ~ 0.3 - 0.4 m for model A-5, ~ 0.1 - 0.25 m for
443 model A-3, and <0.1 m for model A-1. We find that overall, the west coast of Lombok experiences higher tsunamis
444 than the southeast coast of Bali, because it is closer to the tsunami source and the coastline is perpendicular to the
445 source, making it more exposed to the propagating waves. The maximum tsunami height on the west coast of
446 Lombok is ~ 1.8 - 3.7 m for models A-3 and A-5. On the other hand, the more distant and better protected
447 southeastern coast of Bali has a maximum wave height of ~ 1.3 - 2.2 m given the same slip amount, with slightly
448 higher waves within the semi-enclosed bays (Figs. 7d-e).

449 When only the upper half of the fault ramp slips (model B), the uplift patch is narrower and the subsidence region
450 is broader, covering about three quarters of the coasts of Lombok and Bali. Unlike in model A, the headlands at
451 8.38°S are now within the area of subsidence (Fig. 8). This results in an increase in the relative maximum wave
452 height at the headlands, with ~ 2 - 4 m high tsunamis for models B-3 and B-5 (Fig. 8d-e). Similarly, the west coast
453 of Lombok is hit by ~ 1.7 - 3.4 m high tsunamis, while southeastern Bali experiences ~ 0.8 - 2 m high tsunamis for
454 models B-3 and B-5.

455 The two fault models generate similar maximum wave heights along the west coast of Lombok (Fig. 9), while the
456 tsunamis generated by model A are slightly higher than model B along the southeastern coast of Bali (Fig. 10). In
457 both models, however, we consistently observe higher tsunami waves in Lombok compared to Bali. This
458 difference is best observed using the virtual tide gauge records situated near the cities of Mataram and Denpasar.

459

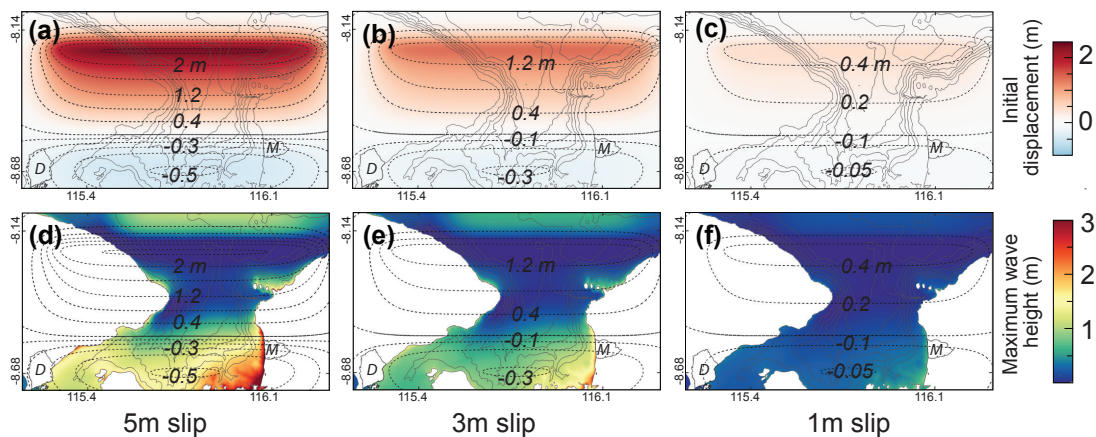
460 3.2 Tsunami time series in Mataram, Lombok and Denpasar, Bali

461 The tide gauge records show that the tsunami arrival times in Mataram and Denpasar are insensitive to the fault
 462 model geometries that we consider. The first and highest wave in Mataram arrives ≤ 9 minutes after the earthquake
 463 and it reaches its peak at ~ 11 minutes, followed by a drawdown at $\sim 15-17$ minutes. Three more waves reach the
 464 coast at ~ 20 , ~ 35 and 45 minutes (1st row, Fig. 11). The first wave in Mataram is $\sim 2.5-2.7$ m high for 5 m slip (A-
 465 5 & B-5), $\sim 1.6-1.7$ m high for 3 m slip (A-3 & B-3), and ≤ 0.6 m high for 1 m slip (A-1 & B-1) (Figs. 9 & 11).
 466 The height of the second wave is $\sim 1.9-2.5$ m, $\sim 1.2-1.5$ m, $\sim 0.4-0.5$ m, respectively, for 5 m, 3 m, and 1 m slip.
 467 The third wave is $\sim 0.6-0.7$ m high for a 5 m slip, $\sim 0.3-0.4$ m for a 3 m slip, $\sim 0.2-0.3$ m for 1 m slip. The last wave
 468 is $\sim 0.1-1.3$, $\sim 0.6-1$, and ≤ 0.2 m, respectively, for 5, 3, and 1 m slips.

469 In Denpasar, the waves are smaller and take longer to arrive (2nd row, Fig. 11). For fault model A, the first wave
 470 arrives at $\sim 12-18$ minutes and reaches its peak at ~ 30 minutes. It is followed by a drawdown at ~ 38 minutes and
 471 a second wave at $\sim 48-53$ minutes. Fault model B has a similar wave pattern with model A, however, its wave
 472 arrival times are slightly later. The first wave in model B arrives at $\sim 23-27$ minutes, followed by a drawdown at
 473 ~ 40 minutes and a second wave at $\sim 52-55$ minutes (Fig. 11). As Denpasar is further from the tsunami source and
 474 has a complex coastline, its wave records are not as uniform as those along the linear coast of Mataram. For both
 475 fault models A and B, relatively higher tsunami waves are generated within the semi-enclosed bay in the northeast
 476 of Denpasar, while lower waves reach southwestwards along the concave coastline (Fig. 10; Gauge 4 on Fig. 11).
 477 Although they have a similar trend, the wave heights generated by model A are slightly higher than model B. For
 478 model A, the maximum wave heights generated are ~ 1.4 m (A-5), ~ 0.9 m (A-3) and ~ 0.3 m (A-1). For model B, the
 479 maximum wave heights generated are ~ 0.8 m (B-5), ~ 0.6 m (B-3) and ≤ 0.2 m (B-1) (Fig. 11).

480

481

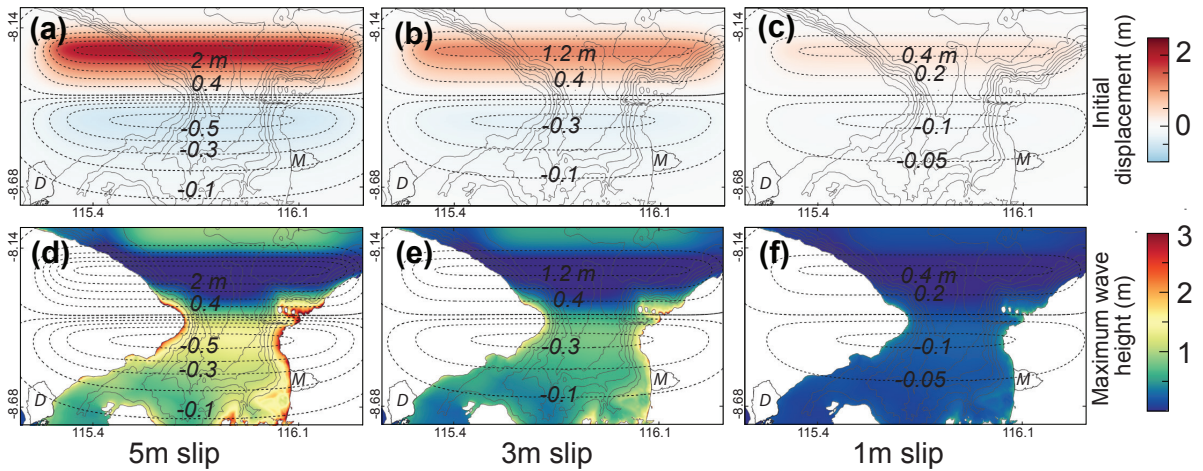


482

Figure 7: Initial surface deformation and maximum wave heights in 1 hr generated by different slip amounts on the full 45-km wide fault ramp (model A). Upper panels (a-c): The coseismic deformation generated by (a) 5 m, (b) 3 m, and (c) 1 m fault slip events result in uplift in the northern half of the islands and subsidence in the south. Lower panels (d-f): Maximum sea surface displacements for (d) 5 m, (e) 3 m, and (f) 1 m fault slip events. Maps are adjusted to show wave heights relative to the post-earthquake land surface rather than initial sea level by subtracting the coseismic displacement (dashed contour lines). The west coast of Lombok is hit by higher tsunami waves than the southeastern coast of Bali. Polygons on land – cities of Denpasar, Bali and Mataram, Lombok. D = Denpasar, M = Mataram.

483

484



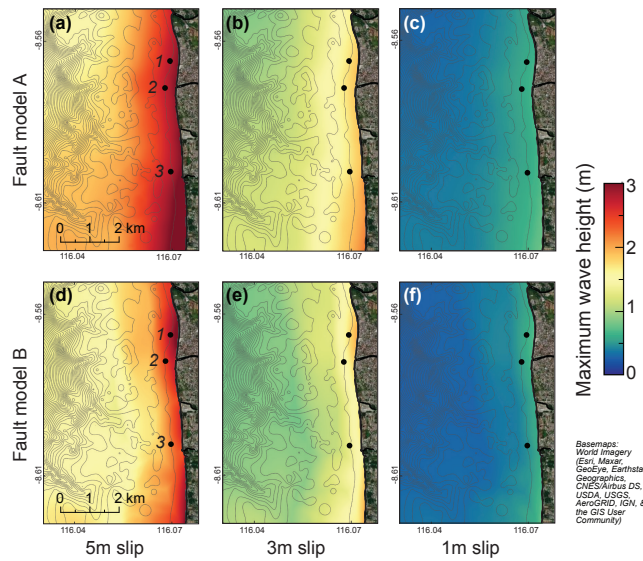
485

Figure 8: Initial surface deformation and maximum wave heights in 1 hr generated by different slip amounts on the upper half of the fault ramp (model B). Upper panels (a-c): The coseismic deformation generated by (a) 5 m, (b) 3 m, and (c) 1 m fault slip events result in a narrow uplift patch in the north and broader subsidence in the south. Lower panels (d-f): Maximum sea surface displacements for (d) 5 m, (e) 3 m, and (f) 1 m fault slip events. Maps are adjusted to show wave heights relative to the post-earthquake land surface rather than initial sea level by subtracting the coseismic displacement (dashed contour lines). The highest waves are concentrated around the headlands of Lombok and Bali at 8.38°S and the mid-west coast of Lombok. Polygons on land – cities of Denpasar, Bali and Mataram, Lombok. D = Denpasar, M = Mataram.

486

487

488

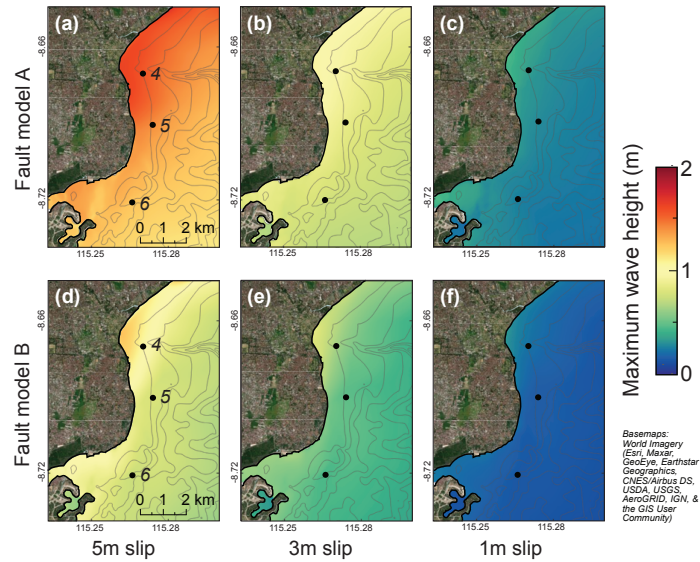


489

Figure 9: Maximum wave heights in Mataram, based on simulations in grid layer 2 (L2, Fig. 6), generated by slip on fault models A (a-c) and B (d-f). Models A-5 (a) and B-5 (d) generate wave heights of ~2.5 to 2.7 m; Models A-3 (b) and

B-3 (e) generate ~1.6 to 1.7 m high waves; the models A-1 (c) and B-1 (f) generate ≤ 0.6 m high waves. Basemaps – World Imagery. Dots – tide gauges.

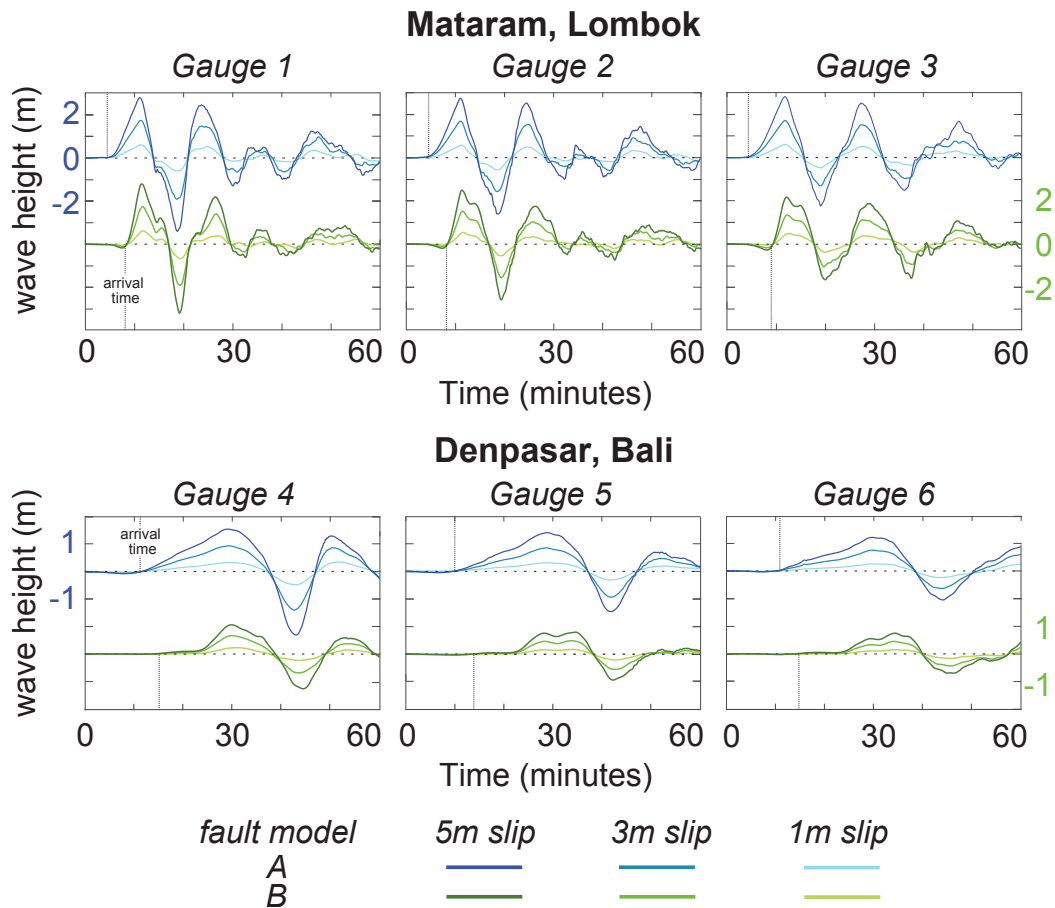
490
491
492



493

Figure 10: Maximum wave heights in Denpasar generated by slip on fault models A (a-c) and B (d-f). The highest tsunami wave heights are located within the semi-enclosed bay on the northeast coast. The maximum wave height near Denpasar range is ~1.4 m for model A-5 (a), ~0.9 m for A-3 (b), and ~0.3 m for A-1 (c). The maximum wave heights are slightly lower in fault model B. It is ~0.8 m for model B-5 (d), ~0.6 m for B-3 (e), and ≤ 0.2 m for B-1 (f). Basemaps – World Imagery. Dots – tide gauges.

494



495

496 **Figure 11:** Sea surface elevation generated by fault models A and B recorded at virtual tide gauges located along the
 497 10 m water depth contours offshore Mataram (gauges 1 to 3) and Denpasar (gauges 4 to 6). The records for fault models
 498 A and B in Mataram are similar in terms of wave heights and arrival times. In Denpasar, the models have similar wave
 499 patterns but the arrival times for model A is slightly earlier than in model B. After the earthquake, the first tsunami in
 500 Mataram arrives at <9 minutes, while in Denpasar it arrives at ~12-18 minutes for model A and ~23-27 minutes. The
 501 peak of the first wave is at ~11 minutes and ~30 minutes in Mataram and Denpasar, respectively.

502

503 3.3 Inundation in Mataram, Lombok

504 Tsunami waves of a given height at the coastline can have variable impact depending on the topography and
 505 infrastructure on land. Because inundation modeling requires a detailed Digital Surface Model for accurate results
 506 and significant computational time, we limit the inundation modeling to the city of Mataram, Lombok, because
 507 this region is densely populated (Fig. 6) and is exposed to the highest waves in our tsunami models. We run the
 508 modeling for fault model A-5 to represent the inundation of the worst-case earthquake scenario used in this study.
 509

510 Based on our results, 5 m of fault slip generates two >2 m high waves followed by two lower waves that hit the
 511 coast at Mataram city (Fig. 11). These waves inundate Mataram with flow depths of generally ≤ 2 m but can reach
 512 as high as 3 m on the southern coast (Figs. 12 and 13). The extent of inundation is ~55-140 m along the northern
 513 to the middle parts of the coast; in the south, it reaches ~230 m. This much wider extent in the south correlates
 514 with a lower density of structures. We interpret that the presence of closely packed structures in the north limits
 515 the inundation further inland. Our results are based on the model assumption that these structures can withstand

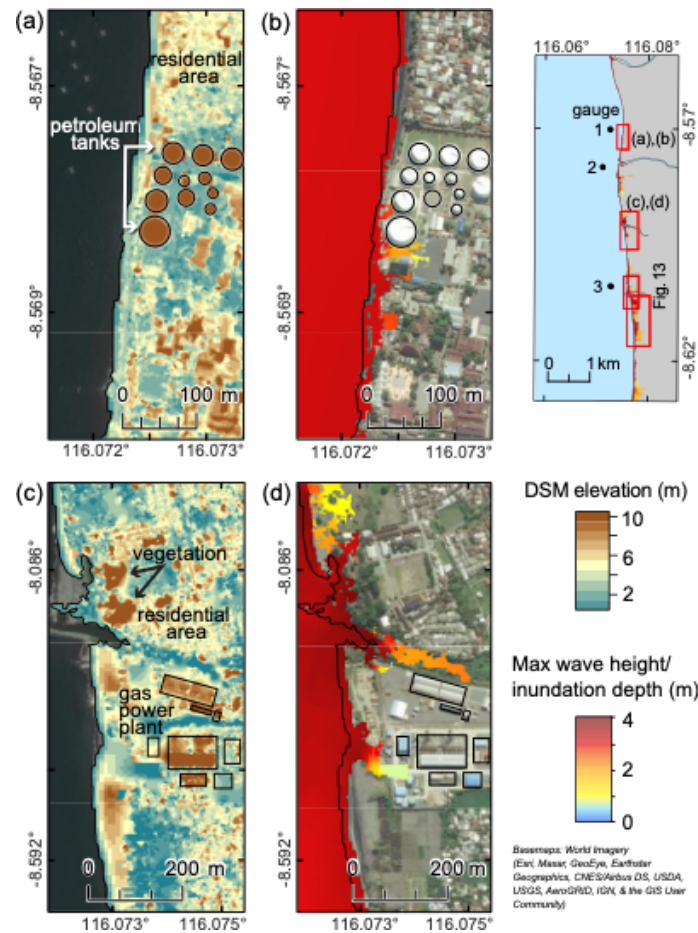
516 the flow; in a real tsunami event, some structures could be destroyed (e.g., 2011 Tohoku earthquake and tsunami,
 517 Mori et al., 2013), which could reduce flow resistance and increase the inundation distance.

518

519 The inundation has limited extent where the beach is narrow and there are dense structures near the coast. For
 520 instance, along the northern (Figs. 12a-b) and mid-southern coasts (Figs 13a-b), inundation is limited to within
 521 the ~15-20 m wide beach, and the closely packed residential structures just behind the beach are not inundated.
 522 At industrial sites where there are more open spaces (Figs. 12a-b and 13a-b), the inundation extent can reach to
 523 ~95-140 m (Figs. 12a-d). When the beach is wider and the structures are further from the coast, the inundation
 524 extends further inland (Figs. 12c-d and 13c-d). We note that in our model, clustered vegetation on the beach is
 525 represented in the DSM as a solid barrier, and thus is able to entirely block the flow (upper part of Fig. 12c-d). In
 526 reality, clustered vegetation can slow but not completely obstruct the flow; the inundation extent at this site is
 527 therefore likely underestimated. Using a digital terrain model, on the other hand, would overestimate the
 528 inundation extent (Muhari et al., 2011). Our results may be more realistic in regions where vegetation is absent,
 529 as in the lower part of Fig. 13a-b, where we model ~175 m inundation. Along the southern coast, the beach is
 530 generally 20-40 m wide and most of the area is farmland; with more open space, the inundation is able to reach
 531 ~230 m inland (Figs. 13c-d).

532

533

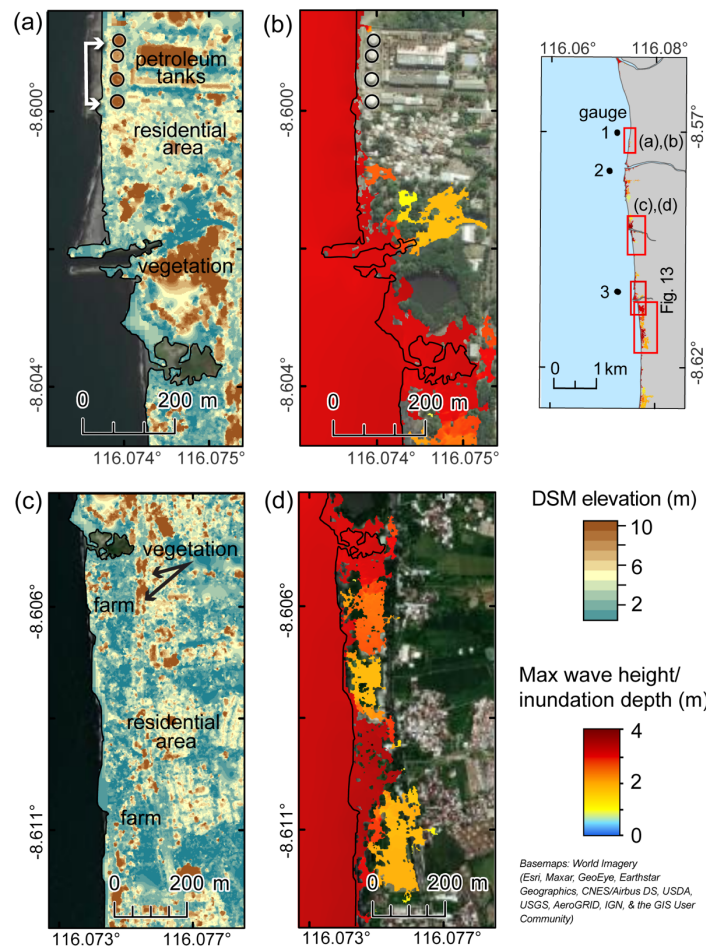


534

Figure 12: The DSM elevation and inundation on the northern coast of Mataram associated with 5 m of coseismic slip on the Flores thrust ramp (model A-5) overlain on World Imagery. Flow depth is generally ≤ 1.5 m. (a-b) The inundation

extent is limited by the high density of structures in residential areas. The inundation reaches ~95 m at the industrial site (circular features are petroleum tanks), where there are more open spaces. (c-d) Inundation may be underestimated in regions where vegetation clusters act in the model as wide barriers to flow but may be more porous, as shown in the upper half of the map. In the area of the gas power plant, where there is less vegetation and the structures are more widely spaced, the inundation extent is ~140 m. Right image – location map of figures.

535



536

537 **Figure 13: The DSM elevation and inundation on the southern coast of Mataram associated with 5 m of coseismic slip**
 538 **on the Flores thrust ramp (model A-5) overlain on World Imagery. (a-b) To the south of the industrial site (with**
 539 **petroleum tanks), the inundation depth is ≤ 1.5 m and the inundation extent is ~175 m. (c-d) In the south, inundation is**
 540 **more extensive, likely because of the lower density of structures and wider open area (beach and farmland). The**
 541 **inundation depth is generally 2-3m and the extent reaches to ~230 m. Right image – location map of figures.**

542

543 4 Conclusions

544 The Flores Thrust is an active south-dipping back-arc fault system traversing north of the Lesser Sunda Islands.
 545 The 2018 Lombok earthquake sequence and prior historical events show that the western part of the fault zone is
 546 capable of generating tsunamigenic earthquakes. In this work, we study the tsunami potential associated with
 547 coseismic slip on the blind fault ramp below Lombok Strait, located between the islands of Lombok and Bali,
 548 using deterministic tsunami modelling. We focus on the tsunami patterns near the capital cities of Mataram,
 549 Lombok and Denpasar, Bali, which both lie on the coasts facing the strait. Our modeling is based on a geologically
 550 constrained model of the fault, informed by the 2018 earthquake sequence. Tsunami propagation is modeled using

551 a high-resolution bathymetry dataset generated by combining data points from the global GEBCO dataset with
552 sounding data digitized from the official nautical charts of Indonesia, interpolated using the Topo to Raster tool
553 in ArcGIS.

554

555 Our results show that fault rupture in this region with 1-5 m of coseismic slip could trigger a tsunami that would
556 hit Mataram, Lombok in ≤ 9 minutes and Denpasar, Bali in ~ 12 -18 minutes with multiple waves. Furthermore,
557 both cities would experience coseismic subsidence of 20-40 cm, exacerbating their exposure to the tsunami hazard
558 and leading to more long-lasting coastal vulnerability. The maximum wave heights in Mataram are 1.6 to 2.7 m
559 for 3-5 m of coseismic slip, while Denpasar has maximum wave heights of 0.6 to 1.4 m. Overall, the coast along
560 Mataram city is more prone than Denpasar to high tsunamis arriving quickly.

561

562 Because Mataram experiences higher wave heights, we also modelled the inundation in this region for our worst-
563 case scenario (5 m slip) using a high-resolution DSM. We found that the inundation extends for ~ 55 -140 m inland
564 with a maximum flow depth of ~ 2 -3 m, and, except in the region just south of the city, where the inundation
565 reaches 230 m. This difference in inundation extent appears to be primarily influenced by the structures present
566 near the coast, which are denser in the north. However, if structures are destroyed by flow, inundation could reach
567 further inland.

568

569 Because of the proximity of the Flores thrust ramp to the coasts of Lombok and Bali, associated tsunamis would
570 hit within < 15 minutes after the earthquake. This early tsunami arrival would mean little time for evacuation. In
571 the case of the 2018 Lombok earthquake, the residents of northern Lombok started evacuation only after a
572 government announcement, and the evacuation took at least 20 minutes (Tsimopoulou et al., 2020). For a potential
573 tsunami in Mataram caused by slip on the Flores thrust, there is insufficient time to wait for an announcement
574 after the earthquake. Hence, raising community awareness about earthquake-generated tsunamis and evacuation
575 plans is important, so that residents will know to respond immediately after experiencing strong ground shaking.
576 Furthermore, the initial polarity of the waves would be positive, and thus there would be no warning signal from
577 drawdown prior to inundation. In addition, a second high wave would hit Mataram coast at ~ 20 minutes,
578 emphasizing the need for continued heightened alert following the first inundation.

579

580 We finally note that some of the structures built along the coast are industrial, with several petroleum tanks and a
581 gas power plant. The impacts of natural disasters can be multiplied when natural events trigger industrial events
582 ('Natural Hazards Triggering Technological Disasters,' or Natech) (Cruz and Suarez-Paba, 2019). Tsunamis in
583 particular have a history of causing Natech events (e.g. (Suppasri et al., 2021); for instance, the 2011 Mw9.1
584 Tohoku earthquake and tsunami led to not only meltdown at the Fukushima-Daichi nuclear power plant, but also
585 fires, explosions, and hazardous materials release at industrial sites (Krausmann and Cruz, 2013). In Mataram,
586 damage to the petroleum tanks, power plant, and other industrial equipment by groundshaking or inundation could
587 trigger Natech events, including fires, explosions, and pollution of the coastal water and associated ecological
588 damage. Evaluating these sites to understand and strengthen their resilience to these hazards should be a priority.

589

590 While most tsunami modeling studies in Indonesia have focused on the hazard associated with large tsunamis
591 triggered by megathrust ruptures, such as the devastating 2004 Indian Ocean earthquake and tsunami (e.g. Wang
592 and Liu, 2007), we highlight here the hazard associated with smaller, local events caused by slip on a back-arc
593 thrust system. One of the challenges with local studies is the need for detailed and accurate fault models and
594 bathymetry datasets. We show that geological information such as regional and nearby seismicity can be combined
595 with bathymetry, topography, and seismic reflection data to model fault geometry, and that a high-resolution
596 bathymetry dataset can be generated by combining globally available bathymetric data with sounding
597 measurements collected for navigation purposes. Specifically, for earthquake-triggered tsunamis in Indonesia, the
598 official nautical charts for Indonesia provide dense measurements offshore shallow coastal cities. Integrating these
599 datasets can provide more accurate forecasts and hazard estimations for both tsunami wave height and arrival
600 time, for local and regional studies, and could be replicated for other fault systems and areas.

601

602 **DATA AVAILABILITY**

603 The animation of the tsunami propagation for the 5 m coseismic slip on the full fault ramp, and the inundation
604 model for Mataram, Lombok can be accessed freely at the Nanyang Technological University Data Repository
605 at: <https://doi.org/10.21979/N9/DZLM5D> and <https://doi.org/10.21979/N9/QKNSKO>, respectively.

606

607 **AUTHOR CONTRIBUTION**

608 RPF, JAH and KEB conceptualized the research. RPF conducted the modeling and the formal analysis. JAH and
609 KEB acquired the funding. JAH supervised the overall work. JAH, KEB and KLH assisted with the fault model
610 setup. LL and ADS assisted with the tsunami modelling. RPF generated the figures. RPF and JAH wrote the
611 original draft. JAH, KEB, KHL, LL and ADS reviewed and edited the manuscript.

612

613 **COMPETING INTERESTS**

614 The authors declare no competing interests.

615

616 **ACKNOWLEDGMENTS**

617 The maps in this paper were made using ArcGIS® software by Esri. The World Ocean Base map is attributed to
618 Esri, GEBCO, NOAA, Garmin, HERE, and other contributors. The World Imagery basemap is attributed to Esri,
619 Maxar, Earthstar Geographics, USDA FSA, USGS, Aerogrid, IGN, IGP, and the GIS User Community. The
620 ArcGIS® and ArcMap™ are the intellectual property of Esri and are used herein under license. Copyright © Esri.
621 All rights reserved. We would like to thank Rishav Mallick for helping in creating figure 4 using the Unicycle
622 code (Moore et al., 2019).

623

624 This research was supported by the Earth Observatory of Singapore via its funding from the National Research
625 Foundation Singapore and the Singapore Ministry of Education under the Research Centres of Excellence
626 initiative. This work comprises EOS contribution number 408. The project was also supported by National Natural
627 Science Foundation China (No 41976197).

628

629

630

631 **REFERENCES**

632

633 Afif, H. and Cipta, A.: Tsunami hazard map in eastern Bali, AIP Conf. Proc., 1658,

634 <https://doi.org/10.1063/1.4915041>, 2015.

635

636 Ammon, C. J., Kanamori, H., and Lay, T.: A great earthquake doublet and seismic stress transfer cycle in the
637 central Kuril islands, *Nature*, 451, 561–565, <https://doi.org/10.1038/nature06521>, 2008.

638

639 Beckers, J. and Lay, T.: Very broadband seismic analysis of the 1992 Flores, Indonesia, earthquake ($M_w = 7.9$),
640 *J. Geophys. Res.*, 100, <https://doi.org/10.1029/95jb01689>, 1995.

641

642 Behrens, J., Løvholt, F., Jalayer, F., Lorito, S., Salgado-Gálvez, M. A., Sørensen, M., Abadie, S., Aguirre-
643 Ayerbe, I., Aniel-Quiroga, I., Babeyko, A., Baiguera, M., Basili, R., Belliazzi, S., Grezio, A., Johnson, K.,
644 Murphy, S., Paris, R., Rafliana, I., De Risi, R., Rossetto, T., Selva, J., Taroni, M., Del Zoppo, M., Armigliato,
645 A., Bureš, V., Cech, P., Cecioni, C., Christodoulides, P., Davies, G., Dias, F., Bayraktar, H. B., González, M.,
646 Gritsevich, M., Guillas, S., Harbitz, C. B., Kânoğlu, U., Macías, J., Papadopoulos, G. A., Polet, J., Romano, F.,
647 Salamon, A., Scala, A., Stepinac, M., Tappin, D. R., Thio, H. K., Tonini, R., Triantafyllou, I., Ulrich, T., Varini,
648 E., Volpe, M., and Vyhmeister, E.: Probabilistic Tsunami Hazard and Risk Analysis: A Review of Research
649 Gaps, *Front. Earth Sci.*, 9, 1–28, <https://doi.org/10.3389/feart.2021.628772>, 2021.

650

651 Van Bemmelen, R. W.: General Geology of Indonesia and adjacent archipelagoes, *Geol. Indones.*, 1949.

652 Bilek, S. L.: Invited review paper: Seismicity along the South American subduction zone: Review of large
653 earthquakes, tsunamis, and subduction zone complexity, 495, 2–14, <https://doi.org/10.1016/j.tecto.2009.02.037>,
654 2010.

655

656 Boekschoten, G. J., Best, M. B., and Putra, K. S.: Balinese reefs in historical context, in: *Proceedings 9th*
657 *International Coral Reef Symposium*, 23–27, 2000.

658

659 Bondarenko, M., Kerr, D., Sorichetta, A., and Tatem, A.: Census/projection-disaggregated gridded population
660 datasets for 189 countries in 2020 using Built-Settlement Growth Model (BSGM) outputs,
661 <https://doi.org/10.5258/SOTON/WP00684>, 2020.

662

663 Bowin, C., Purdy, G. M., Johnston, C., Shor, G., Lawver, L. Hartono, H. M. S., and Jezek, P.: Arc-Continent
664 Collision in Banda Sea Region, *Am. Assoc. Pet. Geol. Bull.*, 64, [https://doi.org/10.1306/2F9193CD-16CE-](https://doi.org/10.1306/2F9193CD-16CE-11D7-8645000102C1865D)
665 [11D7-8645000102C1865D](https://doi.org/10.1306/2F9193CD-16CE-11D7-8645000102C1865D), 1980.

666

667 Chau, K. T. and Lam, K. T. S.: Field observations and numerical simulations of the 2011 Tohoku tsunami using
668 COMCOT, *Comput. Methods Recent Adv. Geomech. - Proc. 14th Int. Conf. Int. Assoc. Comput. Methods*
669 *Recent Adv. Geomech. IACMAG 2014*, 1841–1846, <https://doi.org/10.1201/b17435-326>, 2015.

670

671 Cruz, A. M. and Suarez-Paba, M. C.: Advances in Natech research: An overview, *Prog. Disaster Sci.*, 1, 100013,
672 <https://doi.org/10.1016/j.pdisas.2019.100013>, 2019.

673

674 Darmawan, H., Mutaqin, B. W., Wahyudi, W., Harijoko, A., Wibowo, H. E., Haerani, N., Surmayadi, M.,
675 Syarifudin, S., Jati, R., Suratman, S., and Asriningrum, W.: Topography and structural changes of Anak
676 Krakatau due to the December 2018 catastrophic events, *Indones. J. Geogr.*, 52, 402,
677 <https://doi.org/10.22146/ijg.53740>, 2020.

678

679 Dewey, J. F. and Bird, J. M.: Mountain belts and the new global tectonics, *J. Geophys. Res.*, 75, 2625–2647,
680 <https://doi.org/10.1029/JB075i014p02625>, 1970.

681

682 Felix, R. P., Hubbard, J. A., Moore, J. D. P., and Switzer, A. D.: The Role of Frontal Thrusts in Tsunami
683 Earthquake Generation, *Bull. Seismol. Soc. Am.*, <https://doi.org/10.1785/0120210154>, 2021.

684

685 Fraser, S. A., Power, W. L., Wang, X., Wallace, L. M., Mueller, C., and Johnston, D. M.: Tsunami inundation in
686 Napier, New Zealand, due to local earthquake sources, *Nat. Hazards*, 70, 415–445,
687 <https://doi.org/10.1007/s11069-013-0820-x>, 2014.

688

689 Grezio, A., Babeyko, A., Baptista, M. A., Behrens, J., Costa, A., Davies, G., Geist, E. L., Glimsdal, S.,
690 González, F. I., Griffin, J., Harbitz, C. B., LeVeque, R. J., Lorito, S., Løvholt, F., Omira, R., Mueller, C., Paris,
691 R., Parsons, T., Polet, J., Power, W., Selva, J., Sørensen, M. B., and Thio, H. K.: Probabilistic Tsunami Hazard
692 Analysis: Multiple Sources and Global Applications, *Rev. Geophys.*, 55, 1158–1198,
693 <https://doi.org/10.1002/2017RG000579>, 2017.

694

695 Griffin, J., Latief, H., Kongko, W., Harig, S., Horspool, N., Hanung, R., Rojali, A., Maher, N., Fuchs, A.,
696 Hossen, J., Upi, S., Edi Dewanto, S., Rakowsky, N., and Cummins, P.: An evaluation of onshore digital
697 elevation models for modeling tsunami inundation zones, *Front. Earth Sci.*, 3,
698 <https://doi.org/10.3389/feart.2015.00032>, 2015.

699

700 Griffin, J., Nguyen, N., Cummins, P., and Cipta, A.: Historical earthquakes of the eastern sunda arc: Source
701 mechanisms and intensity-based testing of Indonesia's national seismic hazard assessment, *Bull. Seismol. Soc.*
702 *Am.*, 109, 43–65, <https://doi.org/10.1785/0120180085>, 2019.

703

704 Hall, R. and Spakman, W.: Mantle structure and tectonic history of SE Asia, 658, 14–45,
705 <https://doi.org/10.1016/j.tecto.2015.07.003>, 2015.

706

707 Hamilton, W.: *Tectonics of the Indonesian region*, US Government Printing Office, 1979.

708

709 Hamzah, L., Puspito, N., and Imamura, F.: *Tsunami Catalog Indonesia.pdf*,

710 https://www.jstage.jst.go.jp/article/jnds/22/1/22_1_25/_pdf, 2000.

711

712 Hill, E. M., Borrero, J. C., Huang, Z., Qiu, Q., Banerjee, P., Natawidjaja, D. H., Elosegui, P., Fritz, H. M.,
713 Suwargadi, B. W., Pranantyo, I. R., Li, L. L., Macpherson, K. A., Skanavis, V., Synolakis, C. E., and Sieh, K.:
714 The 2010 Mw 7.8 Mentawai earthquake: Very shallow source of a rare tsunami earthquake determined from
715 tsunami field survey and near-field GPS data, *J. Geophys. Res. Solid Earth*, 117,
716 <https://doi.org/10.1029/2012JB009159>, 2012.

717

718 Horspool, N., Pranantyo, I., Griffin, J., Latief, H., Natawidjaja, D. H., Kongko, W., Cipta, A., Bustaman, B.,
719 Anugrah, S. D., and Thio, H. K.: A probabilistic tsunami hazard assessment for Indonesia, *Nat. Hazards Earth*
720 *Syst. Sci.*, 14, 3105–3122, <https://doi.org/10.5194/nhess-14-3105-2014>, 2014.

721

722 Hutchinson, M. F.: A new procedure for gridding elevation and stream line data with automatic removal of
723 spurious pits, *J. Hydrol.*, 106, 211–232, [https://doi.org/10.1016/0022-1694\(89\)90073-5](https://doi.org/10.1016/0022-1694(89)90073-5), 1989.

724

725 Imamura, F. and Kikuchi, M.: Moment release of the 1992 Flores Island earthquake inferred from tsunami and
726 teleseismic data, *Sci. Tsunami Hazards*, 12, 67–76, 1994.

727

728 Kaiser, G., Scheele, L., Kortenhaus, A., Løvholt, F., Römer, H., and Leschka, S.: The influence of land cover
729 roughness on the results of high resolution tsunami inundation modeling, *Nat. Hazards Earth Syst. Sci.*, 11,
730 2521–2540, <https://doi.org/10.5194/nhess-11-2521-2011>, 2011.

731

732 Kajiura, K.: The Leading Edge of a Tsunami, *Bull. Earthq. Res. Inst.*, 41, 535–571, 1963.

733 Kardoso, R. and Dewi, A. A. C.: Tsunami inundation maps in Mataram City based on tsunami modeling, in:
734 *Proceeding International Conference on Science (ICST)*, 273–278, 2021.

735

736 Koulali, A., Susilo, S., McClusky, S., Meilano, I., Cummins, P., Tregoning, P., Lister, G., Efendi, J., and
737 Syafi'i, M. A.: Crustal strain partitioning and the associated earthquake hazard in the eastern Sunda-Banda Arc,
738 *Geophys. Res. Lett.*, 43, 1943–1949, <https://doi.org/10.1002/2016GL067941>, 2016.

739

740 Krausmann, E. and Cruz, A. M.: Impact of the 11 March 2011, Great East Japan earthquake and tsunami on the
741 chemical industry, *Nat. Hazards*, 67, 811–828, <https://doi.org/10.1007/s11069-013-0607-0>, 2013.

742

743 Kulikov, E. A., Gusiakov, V. K., Ivanova, A. A., and Baranov, B. V.: Numerical tsunami modeling and the
744 bottom relief, *Moscow Univ. Phys. Bull.*, 71, 527–536, <https://doi.org/10.3103/S002713491605012X>, 2016.

745 Kurniawan, T. and Laili, A. F.: Penentuan Area Terdampak "Ketinggian Maksimum Tsunami" di Pulau Bali
746 Berdasarkan Potensi Gempabumi Pembangkit Tsunami Pada Segmen Megathrust Sumba, *J. Dialog dan*
747 *Penanggulangan Bencana*, 10, 93–104, 2019.

748

749 Liu, P. L. F., Cho, Y. S., Yoon, S. B., and Seo, S. N.: Numerical Simulations of the 1960 Chilean Tsunami

750 Propagation and Inundation at Hilo, Hawaii, 99–115, https://doi.org/10.1007/978-94-015-8565-1_7, 1995a.

751 Liu, P. L. F., Cho, Y. S., Briggs, M. J., Kanoglu, U., and Synolakis, C. E.: Runup of solitary waves on a circular
752 Island, *J. Fluid Mech.*, 302, 259–285, <https://doi.org/10.1017/S0022112095004095>, 1995b.

753

754 Løvholt, F., Kühn, D., Bungum, H., Harbitz, C. B., and Glimsdal, S.: Historical tsunamis and present tsunami
755 hazard in eastern Indonesia and the southern Philippines, *J. Geophys. Res. Solid Earth*, 117,
756 <https://doi.org/10.1029/2012JB009425>, 2012.

757

758 Lythgoe, K., Muzli, M., Bradley, K., Wang, T., Nugraha, A. D., Zulfakriza, Z., Widiyantoro, S., and Wei, S.:
759 Thermal squeezing of the seismogenic zone controlled rupture of the volcano-rooted Flores Thrust, *Sci. Adv.*, 7,
760 1–9, <https://doi.org/10.1126/SCIADV.ABE2348>, 2021.

761

762 Marks, K. M. and Smith, W. H. F.: An Evaluation of Publicly Available Global Bathymetry Grids, *Mar.*
763 *Geophys. Res.*, 27, 19–34, <https://doi.org/10.1007/s11001-005-2095-4>, 2006.

764

765 McCaffrey, R. and Nabelek, J.: Earthquakes, gravity, and the origin of the Bali Basin: An example of a Nascent
766 Continental Fold-and-Thrust Belt, *J. Geophys. Res.*, 92, 441, <https://doi.org/10.1029/JB092iB01p00441>, 1987.

767 Moore, J. D. P., Barbot, S., Lindsey, E., Masuti, S., and Muto, J.: [jdpmoore/unicycle: Unicycle](https://doi.org/10.5281/ZENODO.4471162),
768 <https://doi.org/10.5281/ZENODO.4471162>, 2019.

769

770 Muhari, A., Imamura, F., Koshimura, S., and Post, J.: Examination of three practical run-up models for
771 assessing tsunami impact on highly populated areas, *Nat. Hazards Earth Syst. Sci.*, 11, 3107–3123,
772 <https://doi.org/10.5194/nhess-11-3107-2011>, 2011.

773

774 Musson, R. M. W.: A provisional catalogue of historical earthquakes in Indonesia, *Br. Geol. Surv.*, 2012.

775 Nguyen, N., Griffin, J., Cipta, A., and Cummins, P. R.: Indonesia’s Historical Earthquakes: Modelled examples
776 for improving the national hazard map, <https://doi.org/10.11636/record.2015.023>, 2015.

777

778 National Geophysical Data Center / World Data Service: NCEI/WDS Global Historical Tsunami Database.
779 NOAA National Centers for Environmental Information. doi:10.7289/V5PN93H7:

780 Okada, Y.: Internal deformation due to shear and tensile faults in a half-space, *Bull. Seismol. Soc. Am.*, 82,
781 1018–1040, 1992.

782

783 Okal, E. A. and Borrero, J. C.: The “tsunami earthquake” of 1932 June 22 in Manzanillo, Mexico:
784 Seismological study and tsunami simulations, *Geophys. J. Int.*, 187, 1443–1459, <https://doi.org/10.1111/j.1365->
785 [246X.2011.05199.x](https://doi.org/10.1111/j.1365-246X.2011.05199.x), 2011.

786

787 Pradjoko, E., Wardani, L., Wardani, H., Sulistiyono, H., and Sulistiyono, S.: The prediction of tsunami travel
788 time to Mataram City Indonesia based on North Lombok earthquake as the initial condition, *MATEC Web*
789 *Conf.*, 229, 4–8, <https://doi.org/10.1051/matecconf/201822904007>, 2018.

790

791 Pranantyo, I. R., Heidarzadeh, M., and Cummins, P. R.: Complex tsunami hazards in eastern Indonesia from
792 seismic and non-seismic sources: Deterministic modelling based on historical and modern data, *Geosci. Lett.*, 8,
793 20, <https://doi.org/10.1186/s40562-021-00190-y>, 2021.

794

795 Rakowsky, N., Androsov, A., Fuchs, A., Harig, S., Immerz, A., Danilov, S., Hiller, W., and Schröter, J.:
796 Operational tsunami modelling with TsunAWI - Recent developments and applications, *Nat. Hazards Earth*
797 *Syst. Sci.*, 13, 1629–1642, <https://doi.org/10.5194/nhess-13-1629-2013>, 2013.

798

799 Rastogi, B. K. and Jaiswal, R. K.: A Catalog of Tsunamis in the Indian Ocean, *Sci. Tsunami Hazards*, 25, 128–
800 143, 2006.

801

802 Regnier, M., Calmant, S., Pelletier, B., Lagabrielle, Y., and Cabioch, G.: The M_w 7.5 1999 Ambrym
803 earthquake, Vanuatu: A back arc intraplate thrust event, 22, n/a-n/a, <https://doi.org/10.1029/2002TC001422>,
804 2003.

805

806 Rusli, Irjan, and Rudyanto, A.: Pemodelan Tsunami Sebagai Bahan Mitigasi Bencana Studi Kasus Sumenep
807 Dan Kepulauannya, *J. Neutrino*, <https://doi.org/10.18860/neu.v0i0.1639>, 2012.

808

809 Salaree, A., Huang, Y., Ramos, M. D., and Stein, S.: Relative Tsunami Hazard From Segments of Cascadia
810 Subduction Zone For Mw 7.5–9.2 Earthquakes, *Geophys. Res. Lett.*, 48, 1–10,
811 <https://doi.org/10.1029/2021GL094174>, 2021.

812

813 Sallarès, V. and Ranero, C. R.: Upper-plate rigidity determines depth-varying rupture behaviour of megathrust
814 earthquakes, *Nature*, 576, 96–101, <https://doi.org/10.1038/s41586-019-1784-0>, 2019.

815

816 Sallarès, V., Prada, M., Riquelme, S., Meléndez, A., Calahorrano, A., Grevemeyer, I., and Ranero, C. R.: Large
817 slip, long duration, and moderate shaking of the Nicaragua 1992 tsunami earthquake caused by low near-trench
818 rock rigidity, *Sci. Adv.*, 7, <https://doi.org/10.1126/sciadv.abg8659>, 2021.

819

820 Salman, R., Lindsey, E. O., Lythgoe, K. H., Bradley, K., Muzli, M., Yun, S. H., Chin, S. T., Tay, C. W. J.,
821 Costa, F., Wei, S., and Hill, E. M.: Cascading partial rupture of the flores thrust during the 2018 lombok
822 earthquake sequence, indonesia, *Seismol. Res. Lett.*, 91, 2141–2151, <https://doi.org/10.1785/0220190378>, 2020.

823 Satake, K.: Effects of bathymetry on tsunami propagation: Application of ray tracing to tsunamis, *Pure Appl.*
824 *Geophys. PAGEOPH*, 126, 27–36, <https://doi.org/10.1007/BF00876912>, 1988.

825

826 Satake, K.: Linear and nonlinear computations of the 1992 Nicaragua earthquake tsunami, *Pure Appl. Geophys.*,
827 144, 455–470, <https://doi.org/10.1007/BF00874378>, 1995.

828

829 Selva, J., Tonini, R., Molinari, I., Tiberti, M. M., Romano, F., Grezio, A., Melini, D., Piatanesi, A., Basili, R.,

830 and Lorito, S.: Quantification of source uncertainties in Seismic Probabilistic Tsunami Hazard Analysis
831 (SPTHA), *Geophys. J. Int.*, 205, 1780–1803, <https://doi.org/10.1093/gji/ggw107>, 2016.

832

833 Serra, C. S., Martínez-Loriente, S., Gràcia, E., Urgeles, R., Gómez de la Peña, L., Maesano, F. E., Basili, R.,
834 Volpe, M., Romano, F., Scala, A., Piatanesi, A., and Lorito, S.: Sensitivity of Tsunami Scenarios to Complex
835 Fault Geometry and Heterogeneous Slip Distribution: Case-Studies for SW Iberia and NW Morocco, *J.*
836 *Geophys. Res. Solid Earth*, 126, 1–19, <https://doi.org/10.1029/2021JB022127>, 2021.

837

838 Silver, E. A., Reed, D., McCaffrey, R., and Joyodiwiryo, Y.: Back arc thrusting in the Eastern Sunda Arc,
839 Indonesia: A consequence of arc-continent collision, *J. Geophys. Res. Solid Earth*, 88, 7429–7448,
840 <https://doi.org/10.1029/JB088iB09p07429>, 1983.

841

842 Silver, E. A., Breen, N. A., Prasetyo, H., and Hussong, D. M.: Multibeam study of the Flores Backarc Thrust
843 Belt, Indonesia, *J. Geophys. Res. Solid Earth*, 91, 3489–3500, <https://doi.org/10.1029/JB091iB03p03489>, 1986.

844

845 Suardana, A. A. M. A. P., Sugianto, D. N., and Helmi, M.: Study of Characteristics and the Coverage of
846 Tsunami Wave Using 2D Numerical Modeling in the South Coast of Bali, Indonesia, *Indones. J. Ocean. Geogr.*,
847 13, 237–250, 2019.

848

849 Suárez, G., Pardo, M., Domínguez, J., Ponce, L., Montero, W., Boschini, I., and Rojas, W.: The Limón, Costa
850 Rica earthquake of April 22, 1991: Back arc thrusting and collisional tectonics in a subduction environment, 14,
851 518–530, <https://doi.org/10.1029/94TC02546>, 1995.

852

853 Sulaeman, H.: Discovery of Paleotsunami Deposits along Eastern Sunda Arc: Potential for Megathrust
854 Earthquakes in Bali, Brigham Young University, 2018.

855

856 Suppasri, A., Maly, E., Kitamura, M., Syamsidik, Pescaroli, G., Alexander, D., and Imamura, F.: Cascading
857 disasters triggered by tsunami hazards: A perspective for critical infrastructure resilience and disaster risk
858 reduction, *Int. J. Disaster Risk Reduct.*, 66, 102597, <https://doi.org/10.1016/j.ijdr.2021.102597>, 2021.

859

860 Thingbaijam, K. K. S., Mai, P. M., and Goda, K.: New empirical earthquake source-scaling laws, *Bull. Seismol.*
861 *Soc. Am.*, 107, 2225–2246, <https://doi.org/10.1785/0120170017>, 2017.

862

863 Tri Laksono, F. A., Aditama, M. R., Setijadi, R., and Ramadhan, G.: Run-up Height and Flow Depth Simulation
864 of the 2006 South Java Tsunami Using COMCOT on Widarapayung Beach, *IOP Conf. Ser. Mater. Sci. Eng.*,
865 982, 012047, <https://doi.org/10.1088/1757-899X/982/1/012047>, 2020.

866

867 Tsimopoulou, V., Mikami, T., Hossain, T. T., Takagi, H., Esteban, M., and Utama, N. A.: Uncovering unnoticed
868 small-scale tsunamis: field survey in Lombok, Indonesia, following the 2018 earthquakes, *Nat. Hazards*, 103,
869 2045–2070, <https://doi.org/10.1007/s11069-020-04071-z>, 2020.

870

871 Tsuji, Y., Matsutomi, H., Imamura, F., Takeo, M., Kawata, Y., Matsuyama, M., Takahashi, T., Sunarjo, and
872 Harjadi, P.: Damage to coastal villages due to the 1992 Flores Island earthquake tsunami, *Pure Appl. Geophys.*
873 *PAGEOPH*, 144, 481–524, <https://doi.org/10.1007/BF00874380>, 1995.

874

875 Wang, X. and Liu, P. L.-F.: Numerical Simulations of the 2004 Indian Ocean Tsunamis — Coastal Effects, *J.*
876 *Earthq. Tsunami*, 01, 273–297, <https://doi.org/10.1142/s179343110700016x>, 2007.

877

878 Wang, X. and Power, W.: COMCOT: a Tsunami Generation Propagation and Run-up Model, 129 pp., 2011.
879 Wibowo, M., Kongko, W., Hendriyono, W., and Karima, S.: Tsunami Hazard Potential Modeling as Tourism
880 Development Considerations in the North of Lombok Strait, *IOP Conf. Ser. Earth Environ. Sci.*, 832, 012047,
881 <https://doi.org/10.1088/1755-1315/832/1/012047>, 2021a.

882

883 Wibowo, S. B., Hadmoko, D. S., Isnaeni, Y., Farda, N. M., Putri, A. F. S., Nurani, I. W., and Supangkat, S. H.:
884 Spatio-Temporal Distribution of Ground Deformation Due to 2018 Lombok Earthquake Series, *Remote Sens.*,
885 13, 2222, <https://doi.org/10.3390/rs13112222>, 2021b.

886

887 Wilson, K. M. and Power, H. E.: Tsunami Modelling with Static and Dynamic Tides in Drowned River Valleys
888 with Morphological Constrictions, *Pure Appl. Geophys.*, 177, 1595–1616, [https://doi.org/10.1007/s00024-019-](https://doi.org/10.1007/s00024-019-02411-0)
889 02411-0, 2020.

890

891 Yang, X., Singh, S. C., and Tripathi, A.: Did the Flores backarc thrust rupture offshore during the 2018 Lombok
892 earthquake sequence in Indonesia?, *Geophys. J. Int.*, 221, 758–768, <https://doi.org/10.1093/gji/ggaa018>, 2020.

893 Yeh, H., Imamura, F., Synolakis, C., Tsuji, Y., Liu, P., and Shi, S.: The Flores Island tsunamis, *Eos, Trans. Am.*
894 *Geophys. Union*, 74, 369–373, <https://doi.org/10.1029/93EO00381>, 1993.

895

896